

1
2
3
4
5
6
7
8
9
10
11
12
13
14
15
16
17
18
19
20
21
22
23
24
25
26
27
28
29
30
31
32
33
34
35
36
37
38

Body wall structure in the starfish *Asterias rubens*

Liisa M. Blowes^{1,2}, Michaela Egertová¹, Yankai Liu²

Graham R. Davis³, Nick J. Terrill⁴ and Himadri S. Gupta² and Maurice R. Elphick¹

1. School of Biological & Chemical Sciences, Queen Mary University of London,
London, E1 4NS, UK

2. School of Engineering & Materials Science, Queen Mary University of London,
London, E1 4NS, UK

3. Institute of Dentistry, Barts and The London School of Medicine and Dentistry,
Queen Mary University of London, London E1 2AD, UK

4. Diamond Light Source Ltd, Diamond House, Harwell Science and Innovation Campus,
Didcot, Oxfordshire, UK

Correspondence to:

Prof. Maurice Elphick, School of Biological & Chemical Sciences, Queen Mary University of
London, London, E1 4NS, UK; Tel: 0207 882 5290; Fax: 0207 882 7732; E-mail:
m.r.elphick@qmul.ac.uk

OR

Dr. Himadri Gupta, School of Engineering & Materials Science, Queen Mary University of
London, London, E1 4NS, UK; Tel: 0207 882 8867; Fax: 0207 882 3390; E-mail:
h.gupta@qmul.ac.uk

Keywords: body wall, starfish, echinoderm, collagen, ossicle, X-ray microtomography, scanning
synchrotron small-angle X-ray diffraction

SUMMARY

39
40 The body wall of starfish is composed of magnesium calcite ossicles connected by collagenous
41 tissue and muscles and it exhibits remarkable variability in stiffness, which is attributed to the
42 mechanical mutability of the collagenous component. Using the common European starfish *Asterias*
43 *rubens* as an experimental animal, here we have employed a variety of techniques to gain new
44 insights into the structure of the starfish body wall. The structure and organization of muscular and
45 collagenous components of the body wall were analysed using trichrome staining. The muscle
46 system comprises interossicular muscles as well as muscle strands that connect ossicles with the
47 circular muscle layer of the coelomic lining. The collagenous tissue surrounding the ossicle network
48 contains collagen fibres that form loop-shaped straps that wrap around calcite struts near to the
49 surface of ossicles. The 3D architecture of the calcareous endoskeleton was visualized for the first
50 time using X-ray microtomography, revealing the shapes and interactions of different ossicle types.
51 Furthermore, analysis of the anatomical organisation of the ossicles indicates how changes in body
52 shape may be achieved by local contraction/relaxation of interossicular muscles. Scanning
53 synchrotron small-angle X-ray diffraction (SAXD) scans of the starfish aboral body wall and
54 ambulacrum were used to study the collagenous tissue component at the fibrillar level. Collagen
55 fibrils in aboral body wall were found to exhibit variable degrees of alignment, with high levels of
56 alignment probably corresponding to regions where collagenous tissue is under tension. Collagen
57 fibrils in the ambulacrum had a uniformly low degree of orientation, attributed to macrocrimp of the
58 fibrils and the presence of slanted as well as horizontal fibrils connecting antimeric ambulacral
59 ossicles. Body wall collagen fibril D-period lengths were similar to previously reported mammalian
60 D-periods, but were significantly different between the aboral and ambulacral samples. The
61 overlap/D-period length ratio within fibrils was higher than reported for mammalian tissues.
62 Collectively, the data reported here provides new insights into the anatomy of the body wall in *A.*
63 *rubens* and a foundation for further studies investigating the structural basis of the mechanical
64 properties of echinoderm body wall tissue composites.

65 INTRODUCTION

66

67 The phylum Echinodermata comprises five extant classes: the Asteroidea (starfish),
68 Ophiuroidea (brittle stars), Echinoidea (sea urchins and sand dollars), Holothuroidea (sea
69 cucumbers) and Crinoidea (sea lilies and featherstars) (Brusca et al., 2016). A characteristic feature
70 of echinoderms is their endoskeleton, which comprises magnesium calcite ossicles or plates
71 together with varying proportions of associated collagenous and muscular tissue. At one end of the
72 spectrum are sea urchins where the body wall is comprised of fused calcite plates that form a rigid
73 and inflexible endoskeleton (Birenheide et al., 1996, Takemae and Motokawa, 2005, Ribeiro et al.,
74 2011, Ribeiro et al., 2012b, Motokawa and Fuchigami, 2015). At the other end of the spectrum are
75 sea cucumbers, where the body wall is largely comprised of flexible collagenous tissue that contains
76 only a scattering of tiny calcite spicules (Motokawa, 1984, Byrne, 2001). Intermediate compositions
77 are found in asteroids, ophiuroids and crinoids, where the body wall is comprised of calcite ossicles
78 or plates that are interlinked by muscles and collagenous ligaments, which confer skeletal flexibility
79 (Motokawa, 1984, Birenheide and Motokawa, 1996, O'Neill, 1989, Eylers, 1976, Motokawa, 2011).
80 Furthermore, there is variability between starfish species in the proportions of the calcite ossicles,
81 muscle and collagenous tissue in the body wall (Heddle, 1967, Motokawa, 2011).

82 The first detailed investigation of the structure and mechanical properties of the starfish body
83 wall was a study by Eylers (1976) on *Asterias forbesi* Desor, 1848 (Forcipulatida). The structure of
84 the ray skeleton was investigated by analysis of preparations in which the majority of the soft tissue
85 had been dissolved to reveal the architecture of the network of calcite ossicles. Different ossicle
86 types were identified in different regions of the ray, including the ambulacral and adambulacral
87 ossicles on the oral side and the marginal, reticular and carinal ossicles in the aboral body wall.
88 Subsequently, O'Neill (1989) analysed the spatial organisation of ossicles in the aboral body wall of
89 the starfish *Echinaster spinulosus* Verrill, 1869 (Spinulosida) and identified two ossicle types -
90 oblate disks and ellipsoid bars, which form a reticular lattice of hexagonal rings.

91 The ultrastructure of ossicles in the starfish *Pisaster giganteus* Stimpson, 1857 (Forcipulatida)
92 has been investigated using powder X-ray diffraction, infrared spectroscopy, elemental analysis and
93 scanning electron microscopy (SEM) (Gayathri et al., 2007, Martina et al., 2005). This revealed that
94 starfish ossicles are composed of single crystals of macroporous magnesium-rich calcite (stereom),
95 similar to the mineralized skeletal elements of echinoids and some ophiuroids (Addadi et al., 2003,
96 Aizenberg et al., 2001, Long et al., 2014, Raz et al., 2000). X-ray microtomography (Micro-CT) has
97 also been employed to analyse the 3D structure of echinoderm endoskeletons, but the use of this
98 technique has largely focused on fossil specimens (Rahman et al., 2015, Dominguez et al., 2002,
99 Zamora et al., 2012) and only more recently have extant species been examined (Ziegler et al.,
100 2010, Ziegler et al., 2014).

101 The presence of muscles and connective (collagenous) tissue connecting, in parallel, adjacent
102 ossicles of the starfish body wall has been revealed by histochemical staining of thin sections
103 (O'Neill, 1989, Eylers, 1976, Smith, 1936, Hamann, 1885). O'Neill (1989) described the
104 collagenous component of the body wall as a "loosely woven, three-dimensional fabric in which
105 some of the fibres were 'felted' (frayed together)" and where interconnected fibres distribute load
106 across the tissue and prevent delamination under strain. Besides the load bearing collagenous tissue
107 component, O'Neill (1989) also described the interossicular (or "reticular") muscles and muscle
108 layers associated with the coelomic lining of the body wall.

109 Changes in posture of the starfish ray are mediated by the interossicular muscles (Heddle,
110 1967), whereas changes in the stiffness of the body wall are thought to be mediated by
111 interossicular "catch"-type collagenous tissue or mutable collagenous tissue (MCT) (Motokawa,
112 1984, Wilkie, 2005). MCT is a characteristic of all echinoderms, with a unique ability to change
113 stiffness rapidly under the control of the nervous system (Wilkie, 2002, Wilkie, 1996, Takemae and
114 Motokawa, 2005, Wilkie, 2005). The mechanisms of echinoderm MCT are not fully understood.
115 However, it has been proposed that the mutability is conferred not by changes in the mechanical
116 properties of the collagen fibrils but by changes in the stiffness of the interfibrillar matrix (Cluzel et

117 al., 2001, Ribeiro et al., 2012a, Wilkie, 2005). Recently, this mechanism was demonstrated at the
118 nanoscale using sea cucumber dermis as an experimental system (Mo et al., 2016). Furthermore,
119 proteins that may mediate changes in interfibrillar stiffness have also been identified (Motokawa,
120 1984, Trotter et al., 1996, Trotter et al., 1999, Koob et al., 1999, Tipper et al., 2003, Tamori et al.,
121 2006, Yamada et al., 2010, Birenheide et al., 1998).

122 Hitherto, the techniques used to study the soft tissue phase (collagenous and muscle
123 components) of the starfish body wall have been predominantly histological (e.g. trichrome
124 staining) (Heddle, 1967, Eylers, 1976, O'Neill, 1989, Smith, 1936). However, scanning and
125 transmission electron microscopy (SEM and TEM) have also been used to analyse the ultrastructure
126 of fixed echinoderm collagen tissue or extracted fibrils (Trotter et al., 1994, Thurmond and Trotter,
127 1994, Barbaglio et al., 2015, Ribeiro et al., 2011). But fixation and extraction can induce changes in
128 the native structure of the collagen fibrils and therefore alternative methods without use of fixatives
129 are also needed. Microfocus scanning synchrotron small-angle X-ray diffraction (SAXD) is one
130 such technique that has proven to be a powerful and informative approach for analysis of
131 collagenous tissue structure at the nanoscale (Fratzl, 2008, Sasaki and Odajima, 1996a, Puxkandl et
132 al., 2002, Yang et al., 2015, Krauss et al., 2009). Collagenous tissues are amenable for SAXD
133 because collagen molecules are arranged in a highly ordered manner within fibrils, resulting in
134 alternating electron-dense and electron-light regions along the long axis of the fibrils. The
135 combined width of adjacent electron-dense and electron-light regions is known as the D-period,
136 which is ~65-67 nm in mammals, depending on factors such as tissue type and level of hydration
137 (Fratzl, 2008). When collagenous tissue is irradiated with X-rays, the two phase periodic
138 arrangement of electron densities leads to diffraction peaks in the meridional direction, enabling the
139 D-period and fibril orientation to be determined. As long as exposure times to X-rays are not too
140 long (from seconds down to milliseconds depending on the brilliance of the X-ray source), the
141 tissue can be examined in its native state (Jeffries et al., 2015). In this way, SAXD has been used
142 successfully to analyse the structural and mechanical properties of, for example, mammalian

143 tendons, bone and antlers (Karunaratne et al., 2016, Gupta et al., 2006, Zimmermann et al., 2011,
144 Yang et al., 2015). Furthermore, it was use of SAXD that recently enabled interfibrillar stiffening of
145 echinoderm MCT to be demonstrated at the nanoscale, using sea cucumber dermis as an
146 experimental system (Mo et al., 2016).

147 To obtain new insights into relationships between body wall structure and function in
148 starfish, here we have used histology, micro-CT and SAXD to perform a detailed analysis of the
149 structural properties of the body wall in the common European starfish *Asterias rubens* Linnaeus,
150 1758 (Forcipulatida).

151 **MATERIALS AND METHODS**

152

153 **Animals**

154 Starfish (*A. rubens*) used in this study were collected at low tide from Foreness Point near
155 Margate in Kent. Animals were transported in seawater to Queen Mary University of London where
156 they were then maintained in an aquarium with circulating artificial seawater at ~11°C,
157 corresponding to the sea water temperature for this species naturally. Specimens ranging in
158 diameter from 3 to 7 cm were used for studies reported in this paper. Animals were fed periodically
159 with the mussel *Mytilus edulis* Linnaeus, 1758 (Mytiloidea).

160

161 **Masson's trichrome staining**

162 To enable analysis of the histological composition of the body wall in *A. rubens*, Masson's
163 trichrome staining was used, which differentiates collagenous (blue) from non-collagenous (red)
164 tissues. Intact animals or severed rays were fixed for 24 h in Bouin's fixative, which comprised 75
165 ml of saturated picric acid in seawater, 25 ml 40% formaldehyde solution and 5 ml glacial acetic
166 acid. Following fixation, specimens were decalcified at 4°C for 2-5 days in a freshly prepared
167 solution of 1% ascorbic acid in 0.15 M sodium chloride. Prior to fixation, some specimens were
168 narcotized in seawater containing 3.5% added MgCl₂, which causes muscle relaxation (Mayer,
169 1909). This was done to reduce the tissue damage caused during fixation and tissue processing that
170 was observed in untreated specimens. Following fixation and decalcification, starfish rays were
171 dehydrated through an ethanol series, immersed in xylene and then embedded in paraffin wax.
172 Serial transverse sections of rays were prepared using a Leica RM2145 microtome and mounted on
173 chrome alum gelatin coated slides. Following dewaxing in xylene and rehydration, slides were
174 stained using the Masson's trichrome method. Sections were rehydrated and then placed in
175 Weigert's heamatoxylin solution for 10 min and then washed in running tap water for 10 min at
176 room temperature. After rinsing with distilled water, slides were placed in Biebrich scarlet-acid

177 fuchsin solution for 15 min and then washed in distilled water. Differentiation of staining was
178 achieved by placing the slides in phosphomolybdic-phosphotungstic acid solution until collagenous
179 tissue no longer appeared red (normally 10-15 min). Slides were then transferred into aniline blue
180 solution for 5-10 min, followed by washes (3 x 1 min) in distilled water and then a 1-5 min
181 differentiation step in 1% acetic acid. After washing in distilled water, slides were quickly
182 dehydrated in 95% (1 x 10 sec) and 100% ethanol (3 x 10 sec), cleared in xylene and then mounted
183 using DPX, a resin-based mounting medium (Thermo Fisher Scientific Inc.).

184

185 **X-ray microtomography**

186 Micro-CT was used to enable analysis of the structure and organization of the complex
187 network of calcareous ossicles that form the endoskeleton of the body wall in *A. rubens*. Starfish
188 were fixed (overnight at 4°C) with a 4% solution of paraformaldehyde in artificial seawater and
189 then washed in phosphate buffered saline (PBS; pH 7.4). The rays were cut off and embedded in
190 4% low melting point agarose dissolved in PBS, contained within 5 ml polystyrene tubes, which
191 were then stored at 4°C. The complete tubes were scanned on the custom designed MuCAT 2
192 micro-CT scanner at Queen Mary University of London. This uses a high dynamic range CCD
193 camera in time-delay integration mode to achieve accurate, high contrast tomographic images
194 (Davis et al., 2013). The accelerating voltage was set to 40 kV with a tube current of 405 μ A. The
195 voxel size was set to 15 μ m; 1201 projections were recorded in 19 hours (the long scan time is
196 required to obtain a high contrast ratio and two complete scans were required to cover the ~20 mm
197 length of the rays). Immediately following the scan, a multi-element calibration carousel (Evershed
198 et al., 2012) was scanned in order to characterise the X-ray spectrum. Since direct measurement of
199 the X-ray spectrum is almost impossible (with the degree of accuracy required) a modeled estimate
200 of the spectrum is made. Attenuation measurements from the carousel are used to optimize the
201 model to create a good working representation of the spectrum. With *a priori* knowledge of at least
202 the most absorbing components of the specimen, a correction curve can be created that maps the

203 projections derived from polychromatic radiation to an estimate of those that would be derived from
204 monochromatic radiation. This both corrects for beam-hardening errors and allows measurements
205 of mineral concentration to be made from the reconstructed image. While high magnesium calcite is
206 likely the appropriate mineral in the case of starfish ossicles (Gayathri et al., 2007), as we did not
207 know the exact chemical composition and were not interested in absolute mineral concentration
208 measurements, hydroxyapatite mineral was used to create the correction curve. Reconstructed
209 volume images were viewed from different orientations using in-house “Tomview” software and
210 rendered using the Drishti volume rendering package to produce 3D views (Limaye, 2012).

211

212 ***In situ* synchrotron small-angle X-ray diffraction**

213 ***SAXD experiments on starfish aboral body wall and ambulacrum strips***

214 Experiments were performed using the beamline I22 synchrotron light source at Diamond
215 Light Source (DLS; Oxfordshire, UK). Live specimens of *A. rubens* were transported in a portable
216 tank to DLS, where they were maintained in cool seawater until immediately prior to dissection of
217 body wall samples from two individuals. Strips of the midline aboral body wall of rays were
218 prepared using a pair of parallel-blades that were separated by a 6 mm gap. Strips of the
219 ambulacrum on the oral side of rays were prepared by cutting between the rows of ambulacral and
220 adambulacral ossicles on both sides of the ray (see Figs. 1 and 2). The SAXS scans of the
221 ambulacrum and aboral body wall were carried out at different times separated by wide-angle X-ray
222 diffraction measurements on other samples at the same beamline.

223 For static scanning SAXD tests, the strips were placed in a 50 mm × 50 mm plastic clamp,
224 with a hole of 35 mm × 23mm in the centre. The hole was covered with Ultralene film (Spex
225 SamplePrep, Metuchen, NJ, USA), which has minimal X-ray scattering in the small-angle regime.
226 Artificial seawater (ASW, prepared according to the manufacturer’s instructions using Tropic
227 Marin® Sea Salt) was added in between the two layers of film where the sample was held in order
228 to provide a physiological environment for the samples. The edges of the body wall samples were

229 marked with X-ray absorbent lead tape to aid detection of the sample centre when scanning with the
230 X-ray beam.

231 The sample holder was clamped on a 2-axis motorized stage and a synchrotron X-ray beam
232 with a wavelength of 0.8857Å and beam diameter 15 μm was used to acquire the SAXS spectra.
233 Spectra were collected using a silicon hybrid pixel PILATUS 2M detector system (Kraft, 2010).
234 The sample-detector distance was 1008.2 mm for aboral body wall samples and 847.2 mm for
235 ambulacral samples, calculated based on a measurement of a calibration standard consisting of
236 silver behenate. The detector had a 2D resolution of 1475 × 1678 pixels with pixel dimensions of
237 172 × 172 μm².

238 The centre of the sample on the plastic frame was first located by carrying out a 2D X-ray
239 absorption (radiography) scan of the sample across the X-ray beam with a photodiode placed
240 downstream of the sample. The strong X-ray absorption by the lead markers enabled location of
241 regions of interest on the specimen. 2D SAXD area-scans, with 40 and 100 μm x- and y-step
242 distances used for ambulacral and aboral body wall, respectively, were acquired in the regions of
243 interest using software for customized control of motorized stage movement and detector SAXD
244 pattern acquisition, available at the beamline via the GDA open source framework
245 (<http://www.opengda.org/>). Different spatial resolutions were used for the two body regions
246 because of their intrinsically different size. To avoid radiation damage by repeated exposure of the
247 same tissue location to the beam, the 2-axis motorized stage was translated by an offset of 30 μm
248 (~2 × beam diameter) in the x-direction between carrying out the 2D diode and SAXS scan grids.

249

250 ***SAXD data analysis***

251 *Identification of diffraction peaks arising from collagen D-period*

252 2D SAXD spectra were first corrected for air and background scattering by the empty cell,
253 using photodiode measurements of the transmission of the sample and the empty cell, as is standard
254 practice in SAXD data acquisition (Pabisch et al., 2013). The corrected 2D spectra were initially

255 averaged azimuthally across a 0-360° sector (with a wavevector range from 0.2 to 0.9 nm⁻¹) to
256 identify points in the 2D scan where SAXD peaks arising from collagen are present (subsequent
257 more detailed analysis of fibril orientation, D-period and peak intensity is described below). The
258 Bragg peaks arising from the 65-68 nm axial D-period of the collagen fibrils were identified
259 qualitatively from expected positions in the spectrum, with the n = 5th order (at q ~ 0.46 nm⁻¹)
260 being the clearest peak.

261

262 *Determination of collagen fibril orientation*

263 To determine collagen fibril orientation in body wall samples, the angular distribution of the
264 SAXD intensity of the 5th order reflection $I_5(\chi)$ was used. $I_5(\chi)$ was calculated by averaging the
265 intensity radially in a narrow band around the peak position of the 5th order reflection, i.e. over the
266 wavevector range 0.45 – 0.55 nm⁻¹. The intensity profile was calculated for the full angular range in
267 χ from 0 to 360°. To correct for diffuse background scattering, the average of the intensity in two
268 narrow rings (just outside the ring of 0.45-0.55 nm⁻¹ containing the n = 5 reflection) was subtracted
269 from the ring centred on the peak position, following the same procedure as described for bone
270 collagen in Karunaratne et al. (2016). The corrected intensity $I_5(\chi)$ exhibited two peaks separated by
271 180° and hence was fitted to the sum of two Gaussians separated by 180° using the Gnuplot
272 graphics and fitting program (www.gnuplot.info). Peak amplitude, peak width ($\Delta\chi_0$) and peak
273 position (χ_0) were determined from the fit. χ_0 determines mean fibril orientation and the reciprocal
274 of peak width $\left(\frac{1}{\Delta\chi_0}\right)$ was used as a measure of the degree of fibrillar orientation around the mean
275 fibril orientation. Lower values of $\left(\frac{1}{\Delta\chi_0}\right)$ imply a more random dispersion of fibril directions
276 whereas higher values imply a more aligned arrangement.

277 Following identification of fibril direction, the D-period for each 2D pattern was calculated
278 from azimuthally averaged intensity profiles (denoted I_q , with q the radial wavevector; the total
279 intensity of a particular peak order (the integrated intensity under the Bragg peak) will be denoted

280 with a subscript, for example the 5th order peak intensity will be denoted as I_{q_5}). Specifically, the 2D
281 spectra were azimuthally averaged again in a pie-shaped sector centred at the mean fibril
282 orientation, and covering 20° on either sides of χ_0 . This procedure ensures that the signal is not
283 attenuated by including angular sectors, which are far from the principal fibril directions and have
284 no scattering intensity from the collagen meridional peaks. The most clearly visible orders were the
285 fifth ($n = 5, I_{q_5}$) and eighth ($n = 8, I_{q_8}$), with the fifth order having the strongest intensity.

286

287 *Determination of fibril D-period and peak intensity*

288 As the fifth order Bragg peak from the collagen D-period was the most prominent, it was
289 selected for fitting a Gaussian peak function with a linear baseline (background) term for each
290 SAXD spectrum. The peak position q_5 , peak amplitude A_5 , and peak width-at-half-maximum w_{mq_5}
291 were determined from the fits, as reported previously in (Mo et al., 2016). The meridional peak
292 width is influenced by instrumental broadening of the peak due to the finite resolution of the
293 detector. The instrumental broadening of the peak can be calculated from diffraction patterns of
294 collagen fibrils with highly crystalline organisation, such as in dried rat tail tendon or chicken
295 collagen (Krauss et al., 2009). The corrected full-width-at-half-maximum (FWHM) was calculated,
296 as described in Krauss et al. (2009), according to the formula $w_{q_5} = \sqrt{w_{mq_5}^2 - w_{crys}^2}$ where w_{q_5} is
297 the corrected FWHM, w_{mq_5} is the measured FWHM of the sample of interest and w_{crys} is the FWHM
298 of the sample with near crystalline organisation (here chicken collagen was used). The peak width
299 w_{q_5} represents the variability of q_5 at each scan point. As the D-period length is calculated using the
300 formula $D = 5 \times \frac{2\pi}{q_5}$ (as calculated similarly for the third order meridional reflection in bone
301 collagen: e.g. (Karunaratne et al., 2012)), w_{q_5} is also a measure of the variability of D-period length
302 at any scan point. The range of D-values at each scan point can therefore be derived from the above
303 after determining the maximum and minimum q values $q_5 \pm \frac{1}{2}w_{q_5}$, respectively (the use of the half-
304 width as representing maximum and minimum is a convention choice). The azimuthal average of

305 the intensity at the peak position (I_{q_5} and I_{q_8} referring to the intensities of the 5th and 8th order peaks
306 respectively) contains contributions from both the collagen phase as well as from all the other
307 components of the tissue. The diffraction peak intensity is from collagen ($I_{q_{5col}}$) and the background
308 scattering is contributed to by the mineral ($I_{q_{5min}}$) components of the tissue. Therefore to calculate
309 $I_{q_{5col}}$, the background scattering ($I_{q_{5min}}$) was approximated as a linear fall-off over the small q-range
310 around the peak and subtracted from I_{q_5} to get $I_{q_{5col}}$. The linear background scattering was
311 determined by calculating a linear regression over a combination of several points to the left and
312 right of the peak.

313 As not all scan points were on collagen-containing regions, a filtering process was used to
314 identify SAXS patterns with sufficient collagen for analysis, based on the multi-step procedure
315 outlined above. Points with little scattering intensity are expected to give artifactual results for
316 fitting, such as very small or negative peak width, low peak amplitude or very large errors in the fit.
317 After visual inspection of the Bragg peaks of some selected patterns, integrated profiles and fit
318 results, only scan points satisfying the following empirical criteria were determined to have
319 substantial amounts of collagen and were included in the data analysis: i) positive $\Delta\chi_0$, ii) $w_{q_5} >$
320 0.0085 nm^{-1} (very noisy and low intensity $I(q)$ tended to have very small $w_{q_5} < 0.0001 \text{ nm}^{-1}$) and iii)
321 sum of errors (the sum of % error of the peak fit parameters q_{05} , A_5 and w_{q_5}) $< 17 \%$. This
322 corresponded to $\sim 22\%$ of all the scan points.

323

324 ***Determination of the overlap : D-period ratio in collagen fibrils***

325 Structural information on the intrafibrillar arrangement of tropocollagen molecules can be
326 obtained from the differences in peak intensities between the different orders of the SAXD
327 spectrum. Specifically, assuming the gap zone inside the fibril to have a length G and the overlap
328 zone to have a length O and a uniform electron density in each zone, with $O + G = D$, then it can be
329 shown (Sasaki and Odajima, 1996a) that the ratio of the peak intensities of the n_1^{th} peak to that of
330 the n_2^{th} peak is:

331
$$\frac{I_{n_1}}{I_{n_2}} = \left(\frac{n_2}{n_1}\right)^2 \left(\frac{\sin(\pi n_1 \frac{O}{D})}{\sin(\pi n_2 \frac{O}{D})}\right)$$

332 The two most prominent peaks in the radial profile I_q were the 8th and 5th order. Hence, from the
333 ratio of the intensities of the $n_1 = 8^{\text{th}}$ order peak to the $n_2 = 5^{\text{th}}$ order peak (I_{q8}/I_{q5}) the ratio O/D was
334 determined by numerically solving the above equation for O/D, given an experimentally measured
335 intensity ratio. It is noted that the assumption of a constant electron density is likely not strictly
336 accurate, as has been found in vertebrate collagen types (Antipova and Orgel, 2010), but in the
337 absence of a detailed information on the amino acid sequences and structure of collagen in starfish
338 body wall, we use it as an approximation.

339 **RESULTS**

340

341 To facilitate interpretation of data obtained using histological staining, micro-CT and SAXD
342 (see below), figure 1 shows the anatomy of a dissected specimen of *A. rubens*.

343

344 **Histology of the body wall of *Asterias rubens***

345 Figure 2 shows a trichrome stained section of a decalcified ray from *A. rubens*, with the
346 calcite ossicles that are present *in vivo* appearing as voids because of the decalcification process.
347 Here we focus our attention on the structure and organization of collagenous (blue) and non-
348 collagenous (red) tissues that surround and interlink the ossicles, which are shown at higher
349 magnification in Fig. 3.

350 Adjacent ossicles in the body wall are interlinked by muscles and the sizes and shapes of
351 these muscles vary between ossicle types. Examples of the small muscles that link ossicles in the
352 aboral body wall are shown in Fig. 3, which shows interossicular muscles linking adjacent reticular
353 ossicles (Fig. 3A, B). What these images also show is that muscle fibres of the interossicular
354 muscles appear to be wrapped around voids that would be filled by calcite struts near the ossicle
355 surface *in vivo*. In close association with the interossicular muscle is the collagenous tissue that
356 surrounds and also interconnects adjacent ossicles. The collagenous tissue occupies the bulk of the
357 space between ossicles and surrounding ossicles, with fibres forming a dense latticework (Fig. 3A,
358 B). It can clearly be seen that the collagen fibres form loop-shaped straps that wrap around the
359 voids that would be filled by calcite struts near the ossicle surface *in vivo* (Fig. 3C). Indeed the
360 entire surface of each ossicle is penetrated by collagen fibres that project into the ossicle.

361 The coelomic epithelium of the aboral body wall is underlain by two muscle layers. Firstly,
362 a layer of longitudinally orientated muscle, which is thickened along the midline to form what is
363 known as the apical muscle. Secondly, a layer of circularly oriented muscle, from which are derived
364 muscle strands that insert onto the inner surface of body wall ossicles (Fig. 3C).

365 The largest interossicular body wall muscles are the antagonistic pairs of muscles that link
366 adjacent antimeric ambulacral ossicles (abductor supra- and adductor infra-ambulacral muscles) and
367 that link ambulacral and adambulacral ossicles (inner and outer lateral transverse muscles) (Figs. 2,
368 3D), which participate in enabling changes in ray posture (Heddle, 1967). The collagen fibres
369 connecting the antimeric and longitudinally adjacent ambulacral ossicles are oriented
370 predominantly horizontally (Fig. 3D), but slanted fibres connecting longitudinally overlapping
371 ossicles between and within each side of the ambulacrum can also be observed in Fig. 3E. Crimping
372 of collagen fibres in the interambulacral ligament located above the adductor infra-ambulacral
373 muscle can be seen in Fig 3F.

374

375 **X-ray microtomography reveals the 3D architecture of the starfish ray skeleton**

376 Based on data obtained using micro-CT to analyze the ray skeleton of *A. rubens*, here we
377 present images that show for the first time the 3D architecture of the starfish skeleton in
378 unprecedented detail (Fig. 4). A detailed description of the images shown in Fig. 4 is presented in
379 the associated figure legend and therefore here we will focus on a few key observations. What the
380 images show most strikingly is the variety of shapes of the different ossicle types and the geometry
381 of their interactions. Thus, the ambulacral ossicles are elongated, flattened and tightly packed with
382 their aboral “head” region orientated over the adjacent proximal ambulacral ossicle (Fig. 4D). These
383 contrast with the more cuboid-shaped adambulacral ossicles that provide basal support for the
384 ambulacral ossicles (Fig. 4B). The marginal ossicles that form the lateral body wall region are more
385 varied in shape and size but are quite tightly packed. Larger irregular shaped marginal ossicles form
386 longitudinal overlapping rows of ossicles, which are connected radially by overlapping smaller,
387 lozenge-shaped ossicles (Figs. 4B and D). The reticular ossicles that form the aboral skeleton have a
388 similar variety of ossicle shapes and sizes but these form a more open skeletal meshwork than the
389 marginal ossicles (Fig. 4C). Lastly, the carinal ossicles form a single row of overlapping ossicles

390 along the midline of the aboral ray skeleton, arranged like a fallen line of dominos toppled from the
391 tip-end of the ray (Figs. 4 A and B).

392 Another feature that can be observed from the images shown in Fig. 4 are the shapes and
393 sizes of what appear as unfilled gaps where the X-ray attenuation is below the threshold set for the
394 “hard tissue” image rendering, and which is indistinguishable from the surrounding medium but
395 would be filled with tissue *in vivo*. For example, linking the “head” regions of the ambulacral
396 ossicles are several muscles (Fig. 2) and the size and shapes of the spaces occupied by these
397 muscles can be observed in Fig. 4D. Voids that would be filled by a narrow fluid-filled tube linking
398 the tube foot podium and ampulla can also be seen in Fig 4D, where they form two rows on each
399 side of the ambulacrum in an alternating manner with a void proximal or distal to the head region of
400 each pair of adjacent ambulacral ossicles. At the other end of the ambulacral ossicles, it can be seen
401 that their bases insert in a groove formed by adjacent adambulacral ossicles (Figs. 4B-D), i.e. the
402 ambulacral ossicles are not arranged directly above the adambulacral ossicles but are staggered so
403 that these two interacting ossicle types alternate with respect to each other along the length of the
404 ray.

405

406 **X-ray transmission maps of aboral body wall and the ambulacrum reveal the positions of** 407 **ossicles and spines**

408 In order to interpret SAXD data with respect to anatomical organisation of the starfish body
409 wall, X-ray transmission maps were first obtained. Scanning X-ray transmission images of the
410 aboral body wall and ambulacrum revealed their inhomogeneous structure, with regional variation
411 in X-ray transmission and hence conversely X-ray absorption (Figs. 5A1, 5A2; the longitudinal axis
412 of the starfish ray is indicated by an arrow in these figures). Regions with high X-ray absorption
413 correspond with the location of the mineralized ossicles and associated appendages (e.g. spines, * in
414 Fig. 5A1). Thus, the lattice-like structure of the aboral endoskeleton that can be seen with micro-CT
415 (Figs. 4A and 4B) is also revealed in X-ray transmission maps (Fig. 5A1). In Fig. 5A1 the outline of

416 the row of carinal ossicles is indicated with dashed lines and it can be seen that the regions of
417 highest X-ray absorption (blue in Fig. 5A1) in the aboral body wall correspond with the positions of
418 spines located on the outer surface of the body wall. In the ambulacrum, the overall level of X-ray
419 absorption is much higher than in the aboral body wall, consistent with the presence of the regular
420 and densely packed rows of pairs of long ladle-shaped ambulacral ossicles (Fig. 5A2, ambulacral
421 ossicle head, AMOh). However, regions of lower X-ray absorption are evident and these assist in
422 identifying boundaries between adjacent ossicles. The regions of lowest X-ray absorption are along
423 the mid-line of the ambulacrum, which is where the heads of the ambulacral ossicles align and are
424 interlinked by muscles and collagenous tissue (Fig. 5A2).

425

426 **SAXD reveals the inhomogeneous distribution of collagen in the starfish body wall**

427 The amount of collagen present in tissue is proportional to the intensity of the 5th order
428 Bragg peak with the diffuse background scattering ($I_{q_{5min}}$) subtracted from it ($I_{q_{5col}}$, see methods). By
429 mapping the $I_{q_{5col}}$ across the body wall samples (Fig 5B1 and 5B2), the areas with the highest
430 concentrations of collagen (red) can be seen. Note, however, that the intensities shown in Fig 5B1
431 and 5B2 are in arbitrary units and intensities cannot be directly compared between the aboral body
432 wall (Fig. 5B1) and the ambulacral (Fig. 5B2) samples because signal intensity is affected by
433 sample thickness. The large ovoid regions without distinguishable collagen diffraction spectra
434 correspond to voids in aboral body wall skeleton and collagenous tissue that are overlain on the
435 body wall surface by papulae (thin-walled finger-like protrusions that mediate gas exchange in
436 starfish) and pedicellariae (pincer-like organs that remove debris and encrusting organisms from the
437 body wall surface), as seen Fig. 1D. In the ambulacrum, collagen spectra are detectable at scan
438 points along the midline between the antimeric ambulacral ossicles (arrow heads in Fig. 4B1),
439 which corresponds with the position of interossicular ligaments that link the ambulacral ossicles
440 (Figs. 3D, 3E and 3F).

441 A map of the ratio of diffraction intensity from collagen to the mineral scattering intensity
442 (I_{q5col}/ I_{q5min} Fig. 5C1 and 5C2) shows that the background scattering from the ossicles is
443 proportionally higher in the ambulacrum compared to the aboral body wall (note the different
444 scales). This can be attributed to thicker ossicles in the ambulacrum and/or proportionally higher
445 amounts of collagen in the aboral body wall.

446

447 **SAXD reveals collagen fibril orientation and differences in the degree of fibril orientation in**
448 **starfish aboral body wall and ambulacrum**

449 Measurement of the azimuthal intensity distribution of the 5th order reflection $I_5(\chi)$ enabled
450 determination of collagen fibril orientation in body wall samples. Thus, Figs. 5D1 and 5D2 show
451 vector plots overlaid on grayscale X-ray transmission maps, with the orientation of vectors
452 representing mean collagen fibril orientation. In the aboral body wall the carinal ossicles are
453 surrounded by fibrils aligned with the longitudinal axis of the starfish ray (black arrow). Fibrils
454 adjacent to the reticular ossicles are orientated towards the voids in the ossicular lattice (white
455 arrows), perpendicular to the ossicle surface.

456 In addition to fibril orientation, the extent to which fibrils are parallel (called degree of
457 orientation here) can be determined from the inverse of the width of the azimuthal integrated
458 intensity profile ($\frac{1}{\Delta\chi_0}$). Azimuthally wide diffraction peaks (large $\Delta\chi_0 > 10^\circ$) indicate high variation
459 in the angular orientation of fibres. The scaled (from 0-1, normalised using a standard minimum and
460 maximum for all the samples) mean degree of orientation for aboral body wall samples (0.13, SD
461 0.20) was twice that of ambulacrum samples (0.06, SD 0.03). These correspond to azimuthal
462 diffraction peaks with mean FWHM of $\sim 17^\circ$ and $\sim 35^\circ$, respectively. The degree of variation at
463 different scan points is illustrated by the lengths of the vectors in Figs. 5D and 5D'. The longer the
464 vector, the more parallel are the fibres at each scan point. The vector length varies more in the
465 aboral body wall (the standard deviation of the vector length in the aboral samples is nearly 7 times

466 that of ambulacral samples), i.e. the variation in degree of orientation was higher in the aboral body
467 wall samples than in the ambulacrum.

468

469 **D-period length and Overlap/D ratio of collagen fibrils differ between starfish aboral body**
470 **wall and ambulacrum**

471 Collagen fibril D-period lengths (see Fig. 6A, which shows a diagram of collagen fibril
472 organization) calculated using the fifth order meridional Bragg peak position q_5 , for each scanning
473 point with collagen intensity above the threshold revealed a significant difference in D-period
474 length between the aboral body wall and ambulacrum ($P < 0.001$; two tailed t-test assuming equal
475 variance) (Fig. 6B, D-period distribution). The mean D-period for scanning points in aboral body
476 wall was 65.27 nm (SD 0.60, the combined number of scan points from the two aboral body wall
477 samples included in the analysis; $n=504$) and in the ambulacrum was 66.95nm (SD 0.62, $n=269$).
478 The D-period length was also more variable within each scan point in the ambulacral groove than in
479 the aboral body wall. The range of D-values for each scan point was calculated as described in the
480 methods ($w_{m(aboral)} = 0.012 \text{ nm}^{-1}$, $w_{m(ambulacrum)} = 0.015 \text{ nm}^{-1}$, $w_{crys(chicken)} = 0.011 \text{ nm}^{-1}$) and the mean
481 ranges were $D \pm 0.72 \text{ nm}$ for ambulacrum and $D \pm 0.36 \text{ nm}$ for the aboral body wall, again a
482 possible indication of X-rays penetrating through multiple collagenous layers in the ambulacrum
483 with differential D-period lengths.

484 The O/D overlap ratios calculated using the ratio of I_8/I_5 (by numerically solving the
485 following equation for O/D $\frac{I_8}{I_5} = \left(\frac{5}{8}\right)^2 \left(\frac{\sin\left(\frac{\pi 8 O}{D}\right)}{\sin\left(\frac{\pi 5 O}{D}\right)}\right)$) were also significantly different between the two
486 regions of the body wall ($P < 0.001$; two tailed t-test assuming equal variance; Fig. 6C, O/D
487 distribution). One limitation with utilizing the step function and experimentally measured intensity
488 ratios to estimate O/D is the lack of supporting structural data on echinoderm collagens. Therefore,
489 when using the above mentioned equation to solve O/D it was assumed that electron densities
490 within overlap and gap regions were constant and that the starfish collagen O/D ratio would be

491 between 0.4-0.5, i.e. similar to reported O/D values for mammalian collagen fibrils (Sasaki and
492 Odajima, 1996a), as to the best of our knowledge there have been no reported studies of
493 echinoderm collagen fibril organisation being radically different from mammalian fibrils (see
494 discussion for more details). The O/D ratio was lower in the aboral body wall (0.468, SD 0.015)
495 than in the ambulacrum samples (0.479, SD 0.009). If the differences in D-period length and O/D
496 ratio are both taken into account, the average lengths of overlap and gap regions in the aboral body
497 wall are 30.55 and 34.72 nm, respectively ($O + G = D$, therefore $O = 0.468 \times D$ and $G =$
498 $(1 - O) \times D$). Average O and G lengths for the ambulacrum were 32.07 and 34.88 nm, respectively,
499 showing that with a longer D-period the length of the overlap region increases whilst the gap length
500 remains more or less constant.

501

502 **DISCUSSION**

503

504 We report here a detailed analysis of body wall structure in the starfish *A. rubens*,
505 employing histological, micro-CT and SAXD techniques. Use of these complementary approaches
506 has provided new insights into the functional anatomy of the starfish body wall, as discussed below.

507

508 **Trichrome staining reveals the anatomy of body wall interossicular muscles and ligaments in**
509 ***A. rubens***

510 Trichrome staining of sectioned starfish has been employed previously for analysis of the
511 structure and composition of the body wall, revealing that it is a composite of calcite ossicles linked
512 by interossicular muscles and ligaments (O'Neill, 1989, Motokawa, 2011, Wilkie, 2001, Wilkie et
513 al., 1995, Ben Khadra et al., 2015). The application of this histological staining technique to the
514 common European starfish *A. rubens* adds to these body of data. In particular, high magnification
515 photographs show how interossicular ligaments and muscles insert onto adjacent ossicles, with
516 collagen fibrils and muscle fibres, respectively, wrapping around struts near to the ossicle surface
517 (Fig. 4D'), findings that are consistent with a previous study on the longitudinal interambulacral
518 muscles of the starfish *Pycnopodia helianthoides* Brandt, 1835 (Forcipulatida) (Wilkie et al., 1995).
519 No intermediate tendons linking muscles with ossicles were observed. Thus, cavities in the calcite
520 stereom near to the surface of the ossicle contain the loop-shaped straps of both muscle fibres and
521 collagen fibrils (Figs. 3A,B). This anatomical arrangement provides multiple sites of interaction
522 between the soft (muscle and collagen) and hard (ossicle) tissue of the starfish body wall and may
523 enable stiffened collagenous ligaments to bear load when starfish are static and in between changes
524 in posture initiated by muscle contraction.

525 Analysis of the structure of the aboral body wall in the starfish *E. spinulosus* (O'Neill, 1989)
526 revealed that it comprises an ossicular layer consisting of ossicles and collagenous tissue located
527 between inner and outer collagenous dermal layers, muscle and epithelium, with the collagenous

528 tissue thickest in the inner dermal layer. The organisation of collagen fibrils in the ossicular layer
529 resembles an orthogonal web where the bulk of the collagen fibrils surround the ossicles but do not
530 insert directly into them. This contrasts with the body wall of *A. rubens*, where collagenous tissue is
531 closely associated with the ossicles and many fibrils penetrate into the ossicles to form loop-shaped
532 straps around calcite struts, as discussed above. More recently, Motokawa (2011) analysed the
533 structure of the body wall in the starfish *Linckia laevigata* Linnaeus, 1758 (Valvatida), revealing
534 that in this species the aboral body wall has an exceptionally thick inner dermal collagenous layer.
535 By way of comparison, in *A. rubens* the aboral body wall ossicles are evenly surrounded by
536 collagenous tissue without thickening of the inner dermis (Figs. 2, 3; (Wilkie, 2001)). The presence
537 of a thickened inner dermal collagenous layer in *E. spinulosus* and *L. laevigata* accounts for the
538 increased stiffness and rigidity of the body wall in these species by comparison with *Asterias*
539 (Motokawa, 2011, Eylers, 1976, Marrs et al., 2000). Differences in body wall structure in the
540 Asteroidea have been discussed in detail previously with respect to phylogeny, evolutionary
541 success, ecology and habitat, defence strategies, mode of feeding and reproductive behaviour
542 (Feuda and Smith, 2015, Mah and Blake, 2012, Blake, 1990, Gale, 2011). For example, the
543 mechanical properties of the body wall influence the flexibility of the rays limiting and/or enabling
544 specific feeding behavior (Gale, 2013) and the thickened dermal tissue in the sturdy rays of tropical
545 shallow water valvatids and spinulosids such as *L. laevigata* and *E. spinulosus* has also been
546 attributed as an adaptation against extensive predation (Blake, 1983).

547

548 **X-ray microtomography reveals the 3D structure of body wall ossicles in *A. rubens***

549 To the best of our knowledge this is the first study to employ micro-CT to analyse the 3D
550 anatomy of the body wall ossicular skeleton of an extant starfish species. Use of this technique has
551 generated high resolution images that are informative from a functional perspective. The shapes and
552 interactions of the different ossicle types that form the ray body wall in *A. rubens* are revealed in
553 unprecedented detail.

554 The lateral, reticular and carinal ossicles, which form the skeleton of the aboral body wall,
555 form a mesh-like structure with overlapping lozenge-shaped ossicles organized in rings that
556 surround voids in the body wall skeleton. This “loose” arrangement of ossicles is of functional
557 significance for gas exchange because the voids are overlaid by clusters of papulae (Figs. 1, 2),
558 finger-like extendable and retractable exvaginations of the coelomic lining of body wall. The
559 external epithelium and coelomic epithelium of the papulae are only separated by thin layers of
560 collagenous tissue and muscle and thus they provide a large surface area for gas exchange between
561 the coelomic fluid and external seawater (Brusca et al., 2016). The mesh-like organization of
562 ossicles that form the aboral body wall skeleton is also of functional relevance for changes in body
563 posture in *A. rubens*. Thus, the contractile state of small interossicular muscles that link the aboral
564 body wall ossicles (Figs. 3A, B) will determine the shape and size of a ring of ossicles. This can be
565 seen in Fig. 4C, where the shape and size of the voids in aboral skeleton are highly variable,
566 reflecting the particular posture of the ray when the animal was fixed. Changes in the shape and
567 posture of the rays are required for several types of starfish behaviour. For example, when starfish
568 are upturned by strong water currents they exhibit a righting response, during which the rays twist
569 and/or bend to enable the tube feet on the oral side of the ray to gain contact with the substratum
570 (Pollis and Gonor, 1975). Likewise, when starfish feed on prey such as mussels they adopt a
571 humped posture, with the rays bent so that tube feet proximal to the mouth are able to attach to the
572 valves of the mussel and tube feet in the distal region of the rays maintain attachment to the
573 substratum (Norberg and Tedengren, 1995). A similar posture is adopted during spawning (gamete
574 release), increasing the dissemination of gametes in the water column (Himmelman et al., 2008).
575 Furthermore, flexion of rays is aided by contraction of the apical muscle, a midline thickening of
576 the longitudinally orientated muscle beneath the coelomic epithelium (Figs. 2, 3C).

577 In comparison to the aboral ray skeleton, the ossicles that form the oral ambulacral region of
578 the rays in *A. rubens* are very different in their shape, size and packing. Thus, the ambulacral
579 ossicles are long, thin and tightly packed, with their bases inserting in a groove formed by

580 longitudinally adjacent cuboid-shaped adambulacral ossicles. This anatomy can be inferred from
581 detailed analysis of serial sections of starfish rays (Fig. 3) and scanning electron micrographs of
582 individual ossicles (Wilkie et al., 1995), but analysis of images generated from micro-CT is much
583 easier and quicker. Furthermore, the micro-CT data complement histological data in providing 3D
584 representations of ossicle shapes and the “gaps” between adjacent ossicles. For example, it can be
585 seen how the aboral “head” region of each ambulacral ossicle is shaped (Fig. 4D) to accommodate
586 the muscles and ligaments that link antimeric and longitudinally adjacent ossicles (Fig. 3D).
587 Similarly, indentations in the shaft of the ambulacral ossicles (Fig. 4D) accommodate the fluid-
588 filled tubes that connect each tube foot podium with its associated bulb-shaped ampulla (Fig. 2).

589 Both carinal and ambulacral ossicles are organized in an overlapping manner, with each
590 distal ossicle overlapping the more proximal one inclining towards the central disk. This overlap
591 enables the bending, extension and retraction of the whole ray when the apical muscle within the
592 aboral body wall and the interossicular longitudinal muscles in the ambulacrum contract or relax.

593 Heddle (1967) described body wall structure in the starfish *Luidia ciliaris* Philippi, 1837
594 (Paxillosida) and *Astropecten irregularis* Pennant, 1777 (Paxillosida), paying attention to the
595 organisation of antagonistic pairs of muscles involved in postural changes during locomotion and
596 burrowing of the animals. It was noted that these burrowing starfish have three pairs of antagonistic
597 muscles involved in abduction and adduction of the normally A-shaped ambulacral groove. Only
598 two of these pairs can be observed in *A. rubens* – the transverse supra- and infra-ambulacral
599 muscles and inner and outer lateral muscles (Fig. 2). The lack of a third antagonistic muscle pair is
600 explained by the lack of superambulacral ossicles, structures found only in burrowing starfish that
601 are evolutionarily distantly related to the Forcipulata (Heddle, 1967, Feuda and Smith, 2015). The
602 superambulacral ossicles and associated muscles are involved in changing the ray shape from a
603 walking posture to a posture suitable for digging substrate from underneath the animal using tube
604 feet. *A. rubens* is a non-burrowing starfish and only changes its ray shape to crawl into crevices if
605 stranded on the beach at low tide to avoid exposure to air and predators. Contraction of supra-

606 ambulacral and outer lateral abductor muscles flatten the shape of the starfish ray, increasing the
607 angle between antimeric ambulacral ossicles forming the ambulacral arch. Contraction of infra-
608 ambulacral and inner lateral adductor muscles induces a more rounded and tubular ray shape
609 bringing the rows of tube feet directly below the animal enabling locomotion with only vertical
610 stress on tube feet.

611
612 **SAXD reveals properties of collagen in the body wall of *A. rubens*.**

613 Use of trichrome staining revealed the location of collagen in sections of the body wall of *A.*
614 *rubens*, as discussed above. However, there are limitations in this approach to analysis of
615 collagenous tissue. Firstly, only thin ($\sim 10\ \mu\text{m}$) slices of tissue are sampled in each section, so a 3D
616 perspective requires complex and time-consuming reconstructions. Secondly, tissue fixation and
617 processing for histological analysis causes changes in tissue structure (e.g. shrinkage) (Howat and
618 Wilson, 2014) that may affect interpretation of the structural organization of collagen. Both of these
619 limitations are circumvented with the application of the SAXD method to unfixed starfish body
620 wall strips. Furthermore, SAXD can reveal ultrastructural properties of the fibrils (degree of
621 orientation, O/D ratio) that cannot be determined with light/electron microscopy-based histological
622 methods.

623 X-ray absorption maps revealed the positions of spines above reticular ossicles and the
624 shape of the “gaps” between the ambulacral ossicles, aiding the interpretation of the collagen X-ray
625 diffraction data. The SAXD scans themselves revealed an inhomogeneous distribution of collagen
626 within the aboral body wall. Areas lacking detectable amounts of collagen correspond to voids in
627 the body wall skeleton that underlie clusters of papulae on the body wall surface (Figs. 1, 2). The
628 amount of collagenous components in comparison to mineral (ossicular) components was found to
629 be higher in the aboral body wall in comparison to ambulacrum, consistent with the differences in
630 the thickness of the ossicles in the two locations. The 2D orientation of individual collagen fibrils
631 can be observed in high magnification images of trichrome sections (Figs. 3E, F), but SAXD

632 enables quantification of mean fibril orientation *in vivo* and the degree of orientation of collagen
633 fibrils, enabling comparisons between different locations in the body wall. The degree of fibril
634 orientation within the aboral body wall was highly variable between scan points (the standard
635 deviation of the vector length in the aboral samples was nearly 7 times that of ambulacral samples).
636 This probably reflects the complex lattice-like organization of the ossicles in the aboral body wall
637 where some parts of the tissue are under tension (high degree of orientation) and some completely
638 relaxed (dispersed fibril orientation). In contrast, the ambulacral groove fibrils had a uniformly low
639 degree of orientation (the mean vector length; degree of orientation for ambulacral samples was half
640 of the mean length in the aboral body wall; note the different scales in Figs. 5D1 and 5D2). It might
641 be expected that collagen linking the highly regularly organized ambulacral ossicles would have a
642 high degree of orientation. However, the thickness of the sample and the multidirectional fibres and
643 fibrils (Fig. 3E) with macrocrimp (Fig. 3F) connecting antimeric ambulacral ossicles probably
644 explains the uniform mean orientation with low degree of orientation in the ambulacrum.

645 The reported D-value ranges ($65.3\pm 0.6\text{nm}$ for the aboral body wall and $67.0\pm 0.6\text{nm}$ for
646 ambulacral) are similar to the range of D-values reported for mammalian collagen fibrils (65-67nm,
647 (Krauss et al., 2009, Yang et al., 2015, Sasaki and Odajima, 1996a) and sea cucumber and sea
648 urchin fibrils reported by Trotter et al. (1994) ($65.7\pm 0.5\text{ nm}$), but they are higher and less variable
649 than those reported by Ferrario et al. (2017) ($62.7\pm 2.8\text{ nm}$ for sea urchin, $63\pm 4.7\text{ nm}$ for starfish and
650 $66\pm 1.6\text{ nm}$ for sea cucumber) and Ribeiro et al. (2012b) ($59.2\pm 6.2\text{ nm}$ for sea urchin). The variation
651 in D-period length within echinoderms could reflect the differences in techniques (TEM can only be
652 performed on fixed tissue/extracted fibrils, SAXS on the other hand requires no pre-treatment of
653 tissue) and/or differences between species (all the previous echinoderm studies referred to in this
654 paper used TEM images to measure the D-period). The O/D ratios reported here (0.468, SD 0.015
655 for aboral body wall and 0.479, SD 0.009 for ambulacrum) are the first to be determined in an
656 echinoderm. Interestingly, these are higher than previously described O/D ratios of 0.42-0.46

657 (depending on collagen type) for mammalian fibrils (Antipova and Orgel, 2010, Sasaki and
658 Odajima, 1996b); however, the functional significance of this difference remains to be determined.

659 Comparison of the internal structure of collagen fibrils in the ambulacrum and aboral body
660 wall of *A. rubens* revealed a significantly higher D-period length, variability of D at each scan point
661 and O/D ratio in the ambulacrum. The trend is consistent across and between the samples from each
662 body location and possibly reflects differential fibril composition at sites experiencing varying
663 mechanical demands. At least three mechanisms explaining forms of intrafibrillar deformation in
664 response to increasing tension have been described and recognised in the past (Sasaki and Odajima
665 (1996a), see Fig. 6A for reference of fibril structure). Initially, extension of tissue parallel to the
666 main fibril direction straightens crimped fibrils. Thereafter fibrils can deform by three mechanisms
667 (i) homogeneous elongation of individual tropocollagen molecules (the length of D increases, O/D
668 remains the same, refer to Fig. 6A), (ii) molecular slippage where only the gap between
669 longitudinally adjacent molecules increases (no change in D, but decrease in O/D) and/or (iii)
670 inhomogeneous elongation of the molecules (elongation of only gap or overlap regions).
671 Additionally the length of D has been shown to vary between and within tissues even when they are
672 not under tension (Fang et al., 2012).

673 Until now, the correlation between D and O/D has only been studied in the context of
674 changes at a single tissue location during/before and after extension. This study focuses on two
675 different locations with no external strain applied. Therefore, the observed differences in D-values
676 and O/D ratios may not solely or primarily represent differences in the state of tension in the tissue.
677 The structure of fibrils is determined by constituent tropocollagen molecules (e.g. hetero vs
678 homotrimeric and type of collagen alpha chains) (Orgel et al., 2006, Antipova and Orgel, 2010) and
679 the length of D varies between mammalian collagenous tissues (Fang et al., 2012). The differences
680 in the observed D and O/D values between aboral body wall and ambulacrum could therefore arise
681 either from differential strain conditions and/or the molecular structure of the fibrils. Fibrillar
682 collagen isolated from *Asterias amurensis* Lütken, 1871 (Forcipulatida) body wall consists of

683 ($\alpha 1$)₂ $\alpha 2$ heterotrimers, similar to mammalian type I collagen (Kimura et al., 1993). This study,
684 however, does not specify whether the collagen was isolated from whole starfish or aboral body
685 wall only. Nor have any amino acid sequences of *A. amurensis* or *A. rubens* $\alpha 1$ and $\alpha 2$ procollagen
686 chains been determined, to the best of our knowledge. Hence we cannot, at this stage, make any
687 statements about the difference (or not) between aboral and ambulacral collagen molecular
688 structure. We also acknowledge that without structural knowledge of the starfish collagen
689 molecules at the amino acid level, the method of calculating O/D ratios using experimentally
690 measured intensity ratios has some limitations and the interpretation of the data may be reviewed in
691 the future. Nevertheless, the O/D ratios determined here in *A. rubens* give an indication of innate
692 differences between collagenous tissue in different body locations.

693

694 **Future directions**

695 The present study provides detailed insights into ossicle shape and organisation, the structural
696 characteristics of collagenous tissue and the positions of muscles in the body wall of *A. rubens*.
697 Determination of the anatomical organisation of ossicles may provide a basis for experimental
698 investigation of structure-function relationships. This study also highlights the lack of knowledge of
699 *in vitro/vivo* ultrastructural properties of collagen fibrils from non-mammalian animals.
700 Comparative studies between tissues within species and between animals from different clades are
701 required to understand mechanisms such as collagenous tissue mutability. Our study is a first step in
702 this direction.

703 Further studies using *in situ* micromechanical testing during SAXD scanning could bring
704 insights into mechanisms of intrafibrillar deformation and how mechanisms of collagenous tissue
705 mutability work in concert with spatial gradients in collagen fibril composition/re-orientation and
706 the interconnecting ossicular network leading to large scale mechanical and postural changes in
707 starfish. Using the combination of micromechanical testing and SAXD, we have recently shown
708 that the mechanism of collagen mutability in sea cucumbers involves changes in interfibrillar

709 stiffening rather than in any intrinsic changes in the properties of the collagen fibrils themselves
710 (Mo et al., 2016). In inhomogeneous ossicle-tissue networks like the starfish body wall, changes in
711 MCT properties could mechanically affect the links to and between the ossicle network, leading to
712 flexion, torsion etc. Changes in fibril strain and orientation during *in vitro* micromechanical testing
713 can be tracked via changes in the SAXD patterns reflective of four different mechanisms for
714 collagenous tissue elongation: (i) straightening of the fibrillar crimps, (ii) fibril reorientation, (iii)
715 interfibrillar displacement (changes in the interfibrillar cohesion) and (iv) stretching of the fibrils
716 themselves (Gupta, 2008, Sasaki and Odajima, 1996a).

717 Combined information on the material properties, shapes and organization of the ossicles and
718 known material properties of the collagenous and muscle components could also be utilized to build
719 a model of starfish arm movement. The model would provide information about the unique mode
720 of locomotion and postural behavior of starfish. In addition, the model could be used to simulate
721 how the mechanics of composite materials can be modulated through changing the architecture, to
722 make them softer/stiffer and more/less extensible by changing the fibril to mineral component ratio
723 and/or internal structure and spatial organization of one or more of the elements (e.g. the amount of
724 collagen linking the ossicles or the orientation of the fibrils).

725

726 **Conclusion**

727 In conclusion this study provides a detailed description of body wall structure in the starfish
728 *A. rubens*, illustrating the value of a multi-technique approach when characterizing tissue
729 composites. The data obtained provides a structural basis for investigation of the mechanical
730 properties of the starfish body wall both *in vitro* and *in silico*, using *A. rubens* as a model organism.

731 **ACKNOWLEDGEMENTS**

732

733 This work was supported by a Queen Mary University of London PhD studentship awarded to
734 LMB and by grants awarded to HSG and MRE from the Engineering & Physical Sciences Research
735 Council (EPSRC; EP/J501360/1), the Biotechnology and Biological Sciences Research Council
736 (BBSRC; BB/M001644/1) and the Royal Society through the Equipment Grant scheme
737 (SEMF1A6R). HSG thanks Emily Baker (SEMS, QMUL) for acquiring the SEM image of a
738 starfish ossicle (Fig. 4D'). We thank Curtis Horne for assistance with photography of the main
739 image in Fig. 1 and we thank Matouš Elphick and Tomáš Elphick for their enthusiastic assistance
740 with collection of starfish. Lastly, we gratefully acknowledge two anonymous reviewers for helpful
741 comments on this paper.

742

743 **AUTHOR CONTRIBUTIONS**

744 Concept/design, acquisition of data, data analysis/interpretation, drafting of the manuscript: LMB,
745 HSG, MRE; acquisition of data, data analysis: ME, YL, GRD, NJT; all authors contributed to
746 revising of the manuscript and approved the manuscript.

747 **FIGURE LEGENDS**

748

749 **Figure 1. General anatomy of starfish *A. rubens***

750 The main image shows a specimen of the starfish *A. rubens* with one of the rays transversely
751 dissected and with the aboral body wall of two other rays removed to reveal the digestive glands
752 (pyloric caeca, PC) and the ridge of ambulacral ossicle heads (AMOh). Inset A shows a close up of
753 the transverse cross section of the ray with ambulacral ossicles (AMO) and tube feet (TF) on the
754 oral side of the cross section and pyloric caeca attached to the inner side of the aboral body wall.
755 The positions of the apical carinal ossicle (CO) and lateral reticular ossicles (ROs) are labelled.
756 Inset B shows the outer surface of the aboral body wall centered on the mid-line of the arm showing
757 the positions of spines (SPs) that are located over the row of carinal ossicles and clusters of papulae
758 (CPa). Inset C shows a close up of a pedicellaria, a pincer shape defensive organ. Inset D shows a
759 close up of the inner surface of the aboral body wall with voids in the body wall that are overlain by
760 clusters of papulae (CPa) on the outer body wall surface (see inset C). The position of the
761 longitudinally orientated apical muscle (AM) is outlined. The scale bar on the main figure is 1 cm.

762

763 **Figure 2. Trichrome stained transverse section of a decalcified ray from *A. rubens*.**

764 The voids formed by decalcification of the body wall ossicles show the positions and shapes of the
765 different ossicle types: the ambulacral ossicles (AMO), the adambulacral ossicles (ADO), the
766 marginal ossicles (MO), the reticular ossicles (RO) and the carinal ossicle (CO). The red speckling
767 within the ossicle voids are stained cells, which are located in pores between the calcite struts of the
768 ossicle stereom *in vivo*. Surrounding the ossicle network can be seen a dense meshwork of
769 collagenous tissue (blue), which forms the bulk of the soft tissue in the body wall. The
770 interossicular muscles that link adjacent ossicles can also be seen. These are most prominent
771 adorally, where there are large muscles that link adjacent ambulacral ossicles (longitudinal supra-
772 ambulacral muscle, LSM; transverse infra-ambulacral muscle, TIM; transverse supra-ambulacral

773 muscle, TSM) or that link ambulacral ossicles with adambulacral ossicles (inner and outer
774 transverse lateral muscles; TLM; longitudinal lateral muscles, LLM). The smaller interossicular
775 muscles (IOM) linking ossicles of the aboral skeleton are also evident but these are seen more
776 clearly at higher magnification (see Fig. 3). Occupying the coelomic space internal to the body wall
777 can be seen the prominent pair of digestive glands (pyloric caeca, PC), which are connected via
778 mesenteries (*) to the aboral coelomic lining (ACL) of the body wall. The coelomic lining is
779 detached from the body wall in this stained section, which is an artifact probably caused by
780 shrinkage of the body wall dermis during tissue processing. Note that the aboral lining of the
781 coelom is thicker in the midline position due to the presence of the longitudinally oriented apical
782 muscle (AM), which causes aboral flexion of the ray when it contracts *in vivo*. The prominent V-
783 shaped radial nerve cord (RNC) can be seen between the two rows of tube feet podia (TF), which
784 are connected to the intracoelomic bulb-shaped ampullae (AMP) by tubular connections that run
785 between adjacent ambulacral ossicles (as seen here on the right side). Note also other appendages
786 that are associated with the external body wall surface, including spines (SP), pedicellariae (Pe) and
787 papulae (Pa) that overlay voids (V) between the ossicles forming the aboral body wall skeleton.
788 Scale bar is 150 μm .

789

790 **Figure 3. Trichrome stained sections of starfish body wall showing ossicles and associated**
791 **muscles and collagenous tissue.**

792 **A.** Adjacent reticular ossicles (RO) are linked by an interossicular muscle (IOM) and are embedded
793 within a collagenous tissue meshwork (blue). The calcareous struts of the ossicles appear as voids,
794 due to decalcification of the tissue, and the cellular stroma appears red. **B.** High magnification
795 image of adjacent reticular ossicles showing how muscle fibres of an interossicular muscle (IOM)
796 insert between and around strut voids near the surface of each ossicle (white arrows). The wrapping
797 of collagen fibres (blue) around ossicle strut voids (black arrows) can be clearly seen in this image.
798 **C.** Muscle strands (arrows) derived from the circular muscle layer (CML) above the apical muscle

799 (AM; longitudinal muscle) extend through the collagenous inner dermis (blue) and insert on the
800 carinal ossicle (CO). **D.** Ambulacral ossicle heads (AMOHs) are inter-connected by transverse
801 supra-ambulacral muscle (TSM) and longitudinal supra-ambulacral muscles (LSMs). The
802 ambulacral ossicles (AMOs) are furthermore connected by transverse infra-ambulacral muscle
803 (TIM). Other abbreviations as in Fig 2. **E.** Collagen fibres (blue) below the transverse supra-
804 ambulacral muscle (TSM) connect antimeric ambulacral ossicle heads strapping around ossicle
805 struts. **F.** The collagen fibres (blue) above the transverse infra-ambulacral muscle (TIM) have a
806 predominantly transverse horizontal orientation with a macro-crimp (wavy appearance). The scale
807 bar in 3F corresponds to: 50 μm in A, 25 μm in B, 50 μm in C, 100 μm in D, 12.5 μm in E and
808 7.8 μm in F.

809

810 **Figure 4. The ray skeleton of *Asterias rubens*, as revealed by X-ray microtomography.**

811 **A.** Low-magnification overview of the ray skeleton from a top (aboral) view. Along the midline of
812 the aboral skeleton can be seen the row of overlapping carinal ossicles (COs). Either side of the
813 carinal ossicles are a loose meshwork of reticular ossicles (ROs) and through the gaps bounded by
814 rings of reticular ossicles can be seen the two rows of ambulacral ossicles (AMOs) on the oral side
815 of the ray. Note also the numerous spines located external to the ossicle network; three spines
816 located above the carinal ossicles are labeled with arrow heads. **B.** Transverse segment of a starfish
817 ray showing the ambulacral skeleton formed by two rows of ambulacral ossicles (AMO), which are
818 supported orally by the cuboid-shaped adambulacral ossicles (ADO). Lateral to the adambulacral
819 ossicles are the densely packed marginal ossicles (MO). The aboral region of the ray skeleton is
820 formed by a loose meshwork of reticular ossicles (RO) and the single row of carinal ossicles (CO).
821 Spines (SPs) can be seen on the body wall surface **C.** The aboral ray skeleton viewed from its
822 underside, showing the overlapping row of carinal ossicles (COs) along the midline and the loose
823 meshwork of reticular ossicles (ROs) on either side of the carinal ossicles. This image also
824 illustrates how changes in orientation of the carinal and reticular ossicles, mediated *in vivo* by

825 contraction/relaxation of interossicular muscles, affects skeletal structure. Thus, on the left side of
826 the image ossicles form ring-shaped structures, whereas as on the right hand side of the image the
827 ossicles form oblong-shaped structures. **D.** The ambulacral skeleton viewed at high magnification,
828 looking towards the tip of the ray. The image shows how the slender and tightly packed ambulacral
829 ossicles (AMO) are orientated at an angle, leaning away from the tip-end of the ray. Furthermore, it
830 can be seen that the aboral “head” (AMOh) of each ambulacral ossicle overlaps an adjacent ossicle
831 more proximal to the central disk. The large gaps between the adjacent “heads” of ambulacral
832 ossicles (arrow heads and asterisks) are occupied *in vivo* by longitudinally and transversely
833 orientated interossicular muscles, respectively (which can also be seen in Figs. 2 and 3). Dashed
834 lines show where tubular connections of the tube feet and ampullae are located **D’.** Scanning
835 electron micrograph showing the calcite struts and pores of ambulacral ossicle stereom at high
836 magnification. **E.** External view of the marginal ossicles of the body wall. At this high
837 magnification it can be seen that overlapping ossicles with appendages (spines, SP and
838 pedicellariae, Pe) are arranged in longitudinally orientated rows and these ossicles are interlinked
839 radially by smaller ossicles without appendages (arrow heads). Scale bars for A and C, 2 mm; B and
840 D 1 mm; D’ 40 μ m; E 500 μ m.

841

842 **Figure 5. Transmission, I_{q5col} ; I_{q5col} / I_{q5min} ratio and vector maps of *A. rubens* aboral body wall**
843 **and ambulacrum**

844 **A1 and A2.** X-ray transmission maps of an aboral body wall (A1) and an ambulacrum sample (A2).
845 The contour scale corresponds to darker regions as regions with higher density of the tissue (higher
846 absorption). Areas of high density in blue (*) indicate areas of ossicular overlap. The insets are
847 close ups of micro-CT images of corresponding body locations. **B1 and B2.** The Intensity of fifth
848 order Bragg peaks mapped across the aboral (B1) and ambulacrum (B2) samples. Red corresponds
849 to the highest amount of collagen. **C1 and C2.** The ratio of fifth order Bragg peak intensity from
850 collagen fibrils (I_{q5col}), to the intensity of diffuse SAX scattering (which arises mainly from mineral

851 components of the tissue) (I_{q5min}) mapped across the aboral (C1) and ambulacral samples (C2). **D1**
852 **and D2.** Vector and circle plots of collagen fibril structure overlapped with a transmission map of
853 the aboral (D1) and ambulacral samples (D2). The orientations of the vectors are parallel to the
854 orientation of the collagen fibrils. The length of the vector is inversely proportional to $\Delta\chi_0$. The
855 degree of fibril orientation $\left(\frac{1}{\Delta\chi_p}\right)$ increases with the vector length. The scale vector lengths in the
856 bottom left corner correspond to $\left(\frac{1}{\Delta\chi_p}\right)$ of 0.23, 0.46, 0.70 and 0.93 [Au] or $\Delta\chi_0$ of 5, 2.5, 1.67 and
857 1.25 degrees. It is notable that all the vectors in D2 are shorter than the scale vector corresponding
858 to $\Delta\chi_0$ of 5°, in comparison to 8% of vectors in D1 being longer than the scale vector for $\Delta\chi_0$ of 5°.
859

860 **Figure 6. *A. rubens* body wall collagen fibril D-period length and Overlap/D ratio.**

861 A. A simplified diagram of collagen triple helical molecule arrangement within a collagen fibril.
862 The striated collagen fibrils are formed of triple helical collagen molecules that are arranged in a
863 staggered manner leading to electron dense and light regions (overlap, O; gap, G). The combined
864 length of one overlap and gap region equals a D-period (D). The length of the D-period and overlap
865 to D ratio (O/D) can be used as a measure to characterise collagen fibrils. B. The histogram shows
866 the distribution of D-period length in aboral body wall (red solid line) and ambulacral groove (black
867 dotted line) divided in bins of $D < 64.5$ nm; $64.5 \text{ nm} \leq D < 65.5$ nm, $65.5 \text{ nm} \leq D < 66.5$ nm, 66.5
868 $\text{nm} \leq D < 67.5$ nm, $67.5 \text{ nm} \leq D < 68.5$ nm and $68.5 \text{ nm} \leq D < 69.5$ nm. Aboral body wall collagen
869 fibrils have a lower mean D-period than ambulacral ones. C. The histogram shows the distribution
870 of O/D ratios in aboral body wall (red solid line) and ambulacral groove (black dotted line) divided
871 in bins with 0.01 ratio intervals. A lower O/D ratio is observed for the aboral body wall relative to
872 the ambulacrum.

873 **REFERENCES**

- 874 Addadi L, Raz S & Weiner S (2003). Taking advantage of disorder: Amorphous calcium carbonate
875 and its roles in biomineralization. *Advanced Materials*, 15, 959-970.
- 876 Aizenberg J, Tkachenko A, Weiner S, Addadi L & Hendler G (2001). Calcitic microlenses as part
877 of the photoreceptor system in brittlestars. *Nature*, 412, 819-822.
- 878 Antipova O & Orgel JPRO (2010). In situ D-periodic molecular structure of type II collagen. *The*
879 *Journal of biological chemistry*, 285, 7087-7096.
- 880 Barbaglio A, Tricarico S, Ribeiro AR, et al. (2015). Ultrastructural and biochemical
881 characterization of mechanically adaptable collagenous structures in the edible sea urchin
882 *Paracentrotus lividus*. *Zoology (Jena)*, 118, 147-60.
- 883 Ben Khadra Y, Ferrario C, Di Benedetto C, et al. (2015). Re-growth, morphogenesis, and
884 differentiation during starfish arm regeneration. *Wound repair and regeneration* : official
885 publication of the Wound Healing Society [and] the European Tissue Repair Society, 23,
886 623-34.
- 887 Birenheide R & Motokawa T (1996). Contractile connective tissue in crinoids. *The Biological*
888 *bulletin*, 191, 1-4.
- 889 Birenheide R, Tamori M, Motokawa T, et al. (1998). Peptides controlling stiffness of connective
890 tissue in sea cucumbers. *The Biological bulletin*, 194, 253-9.
- 891 Birenheide R, Tsuchi A & Motokawa T (1996). To be stiff or to be soft - The dilemma of the
892 echinoid tooth ligament. II. Mechanical properties. *Biol Bull-US*, 190, 231-236.
- 893 Blake DB (1990). Adaptive zones of the class Asteroidea (Echinodermata). *Bulletin of Marine*
894 *Science*, 46, 701-718.
- 895 Brusca RC, Moore W & Shuster SM (2016). *Invertebrates*, Third Edition, U.S.A, Sinauer
896 Associates.
- 897 Byrne M (2001). The morphology of autotomy structures in the sea cucumber *Eupentacta*
898 *quinquesemita* before and during evisceration. *Journal of Experimental Biology*, 204, 849-
899 863.
- 900 Cluzel C, Lethias C, Humbert F, Garrone R & Exposito JY (2001). Characterization of fibrosurfin,
901 an interfibrillar component of sea urchin catch connective tissues. *The Journal of biological*
902 *chemistry*, 276, 18108-14.
- 903 Davis GR, Evershed ANZ & Mills D (2013). Quantitative high contrast X-ray microtomography for
904 dental research. *J Dent*, 41, 475-482.
- 905 Dominguez P, Jacobson AG & Jefferies RPS (2002). Paired gill slits in a fossil with a calcite
906 skeleton. *Nature*, 417, 841-844.
- 907 Evershed ANZ, Mills D & Davis G (2012). Multi-species beam hardening calibration device for X-
908 ray microtomography. In: Stock SR (ed.) *Developments in X-Ray Tomography VIII*,
909 85061N San Diego, California, USA
- 910 Eylers JP (1976). Aspects of skeletal mechanics of the starfish *Asterias forbesii*. *Journal of*
911 *Morphology*, 149, 353-367.
- 912 Fang M, Goldstein EL, Turner AS, et al. (2012). Type I collagen D-spacing in fibril bundles of
913 dermis, tendon, and bone: Bridging between nano- and micro-level tissue hierarchy. *ACS*
914 *Nano*, 6, 9503-9514.
- 915 Ferrario C, Leggio L, Leone R, et al. (2017). Marine-derived collagen biomaterials from
916 echinoderm connective tissues. *Mar Environ Res* (in press).
- 917 Feuda R & Smith AB (2015). Phylogenetic signal dissection identifies the root of starfishes. *PloS*
918 *one*, 10, e0123331.
- 919 Fratzl P (ed.) (2008). *Collagen Structure and Mechanics*: Springer US.
- 920 Gale AS (2011). The Phylogeny of Post-Palaeozoic Asteroidea (Neoasteroidea, Echinodermata).
921 *Special Papers in Palaeontology*, 85, 1-112.

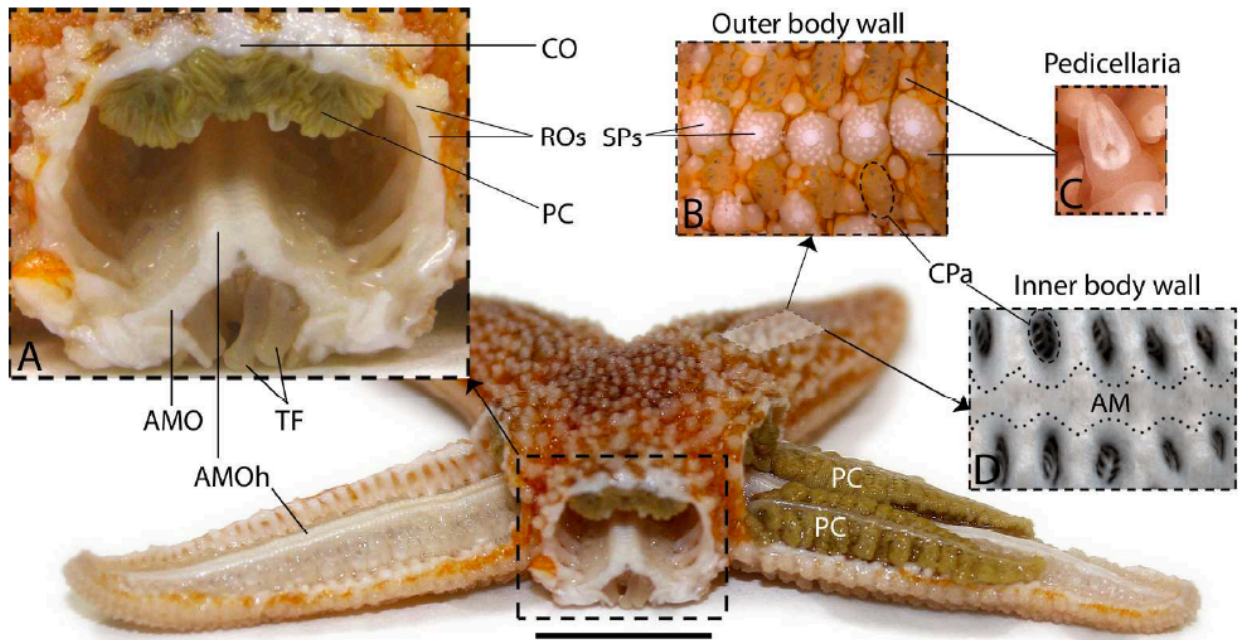
- 922 Gayathri S, Lakshminarayanan R, Weaver JC & Morse DE (2007). *In vitro* study of magnesium-
 923 calcite biomineralization in the skeletal materials of the seastar *Pisaster giganteus*.
 924 Chemistry : a European journal, 13, 3262-3268.
- 925 Gupta HS (2008). Nanoscale Deformation Mechanisms in Collagen. In: Fratzl P (ed.) Collagen:
 926 Structure and Mechanics. Boston, MA: Springer US.
- 927 Gupta HS, Seto J, Wagermaier W, et al. (2006). Cooperative deformation of mineral and collagen
 928 in bone at the nanoscale. PNAS USA, 103, 17741-17746.
- 929 Hamann O (1885). Die Asteriden, anatomisch und histologisch untersucht, Jena, Germany, Verlag
 930 von Gustav Fischer.
- 931 Heddle D (1967). Versatility of movement and the origin of the asteroids. In: Millott N (ed.)
 932 Echinoderm Biology, the proceedings of a Symposia of the Zoological Society of London,
 933 No 20 Bristol, UK: Academic Press Inc. (London) Ltd.
- 934 Himmelman JH, Dumont CP, Gaymer CF, Vallières C & Drolet D (2008). Spawning synchrony
 935 and aggregative behaviour of cold-water echinoderms during multi-species mass spawnings.
 936 Marine Ecology Progress Series, 361, 161-168.
- 937 Howat WJ & Wilson BA (2014). Tissue fixation and the effect of molecular fixatives on
 938 downstream staining procedures. Methods, 70, 12-19.
- 939 Jeffries CM, Graewert MA, Svergun DI & Blanchet CE (2015). Limiting radiation damage for
 940 high-brilliance biological solution scattering: practical experience at the EMBL P12
 941 beamline PETRAIII. Journal of synchrotron radiation, 22, 273-9.
- 942 Karunaratne A, Esapa CR, Hiller J, et al. (2012). Significant deterioration in nanomechanical
 943 quality occurs through incomplete extrafibrillar mineralization in rachitic bone: Evidence
 944 from in-situ synchrotron X-ray scattering and backscattered electron imaging. Journal of
 945 Bone and Mineral Research, 27, 876-890.
- 946 Karunaratne A, Xi L, Bentley L, et al. (2016). Multiscale alterations in bone matrix quality
 947 increased fragility in steroid induced osteoporosis. Bone, 84, 15-24.
- 948 Kimura S, Omura Y, Ishida M & Shirai H (1993). Molecular characterization of fibrillar collagen
 949 from the body wall of starfish *Asterias amurensis*. Comparative Biochemistry and
 950 Physiology Part B: Comparative Biochemistry, 104, 663-668.
- 951 Koob TJ, Koob-Emunds MM & Trotter JA (1999). Cell-derived stiffening and plasticizing factors
 952 in sea cucumber (*Cucumaria frondosa*) dermis. The Journal of experimental biology, 202
 953 (Pt 17), 2291-301.
- 954 Kraft P. (2010). PILATUS 2M a detector for small angle X-ray scattering. Diss , Eidgenössische
 955 Technische Hochschule ETH Zürich, Nr 18466, 2010, ETH.
- 956 Krauss S, Fratzl P, Seto J, et al. (2009). Inhomogeneous fibril stretching in antler starts after
 957 macroscopic yielding: Indication for a nanoscale toughening mechanism. Bone, 44, 1105-
 958 1110.
- 959 Limaye A (2012). Drishti: a volume exploration and presentation tool. In: Stock SR (ed.)
 960 Developments in X-Ray Tomography VIII. San Diego, California, USA.
- 961 Long X, Ma Y & Qi L (2014). Biogenic and synthetic high magnesium calcite – A review. Journal
 962 of Structural Biology, 185, 1-14.
- 963 Mah CL & Blake DB (2012). Global Diversity and Phylogeny of the Asteroidea (Echinodermata).
 964 PloS one, 7, e35644.
- 965 Marrs SJ, Wilkie IC, Skold M, Maclaren WM & MacKenzie JD (2000). Size-related aspects of arm
 966 damage, tissue mechanics, and autotomy in the starfish *Asterias rubens*. Marine Biology,
 967 137, 59-70.
- 968 Martina M, Subramanyam G, Weaver JC, et al. (2005). Developing macroporous bicontinuous
 969 materials as scaffolds for tissue engineering. Biomaterials, 26, 5609-16.
- 970 Mayer AG (1909). On the use of magnesium in stupefying marine animals. The Biological
 971 bulletin, 17, 341-342.
- 972 Mo J, Prévost SF, Blowes LM, et al. (2016). Interfibrillar stiffening of echinoderm mutable
 973 collagenous tissue demonstrated at the nanoscale. PNAS, 113, E6362-E6371.

- 974 Motokawa T (1984). Connective tissue catch in Echinoderms. *Biol Rev*, 59, 255-270.
- 975 Motokawa T (2011). Mechanical mutability in connective tissue of starfish body wall. *The*
976 *Biological bulletin*, 221, 280-9.
- 977 Motokawa T & Fuchigami Y (2015). Coordination between catch connective tissue and muscles
978 through nerves in the spine joint of the sea urchin *Diadema setosum*. *The Journal of*
979 *experimental biology*, 218, 703-10.
- 980 Norberg J & Tedengren M (1995). Attack behaviour and predatory success of *Asterias rubens* L.
981 related to differences in size and morphology of the prey mussel *Mytilus edulis* L. *Journal of*
982 *Experimental Marine Biology and Ecology*, 186, 207-220.
- 983 O'Neill P (1989). Structure and mechanics of starfish body wall. *The Journal of experimental*
984 *biology*, 147, 53-89.
- 985 Orgel JPRO, Irving TC, Miller A & Wess TJ (2006). Microfibrillar structure of type I collagen in
986 situ. *PNAS USA*, 103, 9001-9005.
- 987 Pabisch S, Wagermaier W, Zander T, Li C & Fratzl P (2013). Chapter 18 - Imaging the
988 nanostructure of bone and dentin through small- and wide-angle X-ray scattering. In: James
989 JDY (ed.) *Methods in enzymology*. Academic Press.
- 990 Pollis I & Gonor J (1975). Behavioral aspects of righting in two asteroids from the Pacific coast of
991 North America. *The Biological bulletin*, 148, 68-84.
- 992 Puxkandl R, Zizak I, Paris O, et al. (2002). Viscoelastic properties of collagen: synchrotron
993 radiation investigations and structural model. *Philosophical Transactions of the Royal*
994 *Society B: Biological Sciences*, 357, 191-197.
- 995 Rahman IA, Belaústegui Z, Zamora S, et al. (2015). Miocene Clypeaster from Valencia (E Spain):
996 Insights into the taphonomy and ichnology of bioeroded echinoids using X-ray micro-
997 tomography. *Palaeogeography, Palaeoclimatology, Palaeoecology*, 438, 168-179.
- 998 Raz S, Weiner S & Addadi L (2000). Formation of high-magnesian calcites via an amorphous
999 precursor phase: Possible biological implications. *Advanced Materials*, 12, 38-42.
- 1000 Ribeiro AR, Barbaglio A, Benedetto CD, et al. (2011). New insights into mutable collagenous
1001 tissue: correlations between the microstructure and mechanical state of a sea-urchin
1002 ligament. *PloS one*, 6, e24822.
- 1003 Ribeiro AR, Barbaglio A, Oliveira MJ, et al. (2012a). Matrix metalloproteinases in a sea urchin
1004 ligament with adaptable mechanical properties. *PloS one*, 7, e49016.
- 1005 Ribeiro AR, Barbaglio A, Oliveira MJ, et al. (2012b). Correlations between the biochemistry and
1006 mechanical states of a sea-urchin ligament: a mutable collagenous structure. *Biointerphases*,
1007 7, 38.
- 1008 Sasaki N & Odajima S (1996a). Elongation mechanism of collagen fibrils and force-strain relations
1009 of tendon at each level of structural hierarchy. *J Biomech*, 29, 1131-6.
- 1010 Sasaki N & Odajima S (1996b). Stress-strain curve and Young's modulus of a collagen molecule as
1011 determined by the X-ray diffraction technique. *J Biomech*, 29, 655-8.
- 1012 Smith JE (1936). On the nervous system of the starfish *Marthasterias glacialis* (L.) *Philosophical*
1013 *transactions of the Royal Society of London Series B, Biological sciences*, 227, 111-173.
- 1014 Takemae N & Motokawa T (2005). Mechanical properties of the isolated catch apparatus of the sea
1015 urchin spine joint: Muscle fibers do not contribute to passive stiffness changes. *Biol Bull-*
1016 *Us*, 208, 29-35.
- 1017 Tamori M, Yamada A, Nishida N, et al. (2006). Tensilin-like stiffening protein from *Holothuria*
1018 *leucospilota* does not induce the stiffest state of catch connective tissue. *The Journal of*
1019 *experimental biology*, 209, 1594-602.
- 1020 Thurmond FA & Trotter JA (1994). Native collagen fibrils from echinoderms are molecularly
1021 bipolar. *Journal of molecular biology*, 235, 73-9.
- 1022 Tipper JP, Lyons-Levy G, Atkinson MA & Trotter JA (2003). Purification, characterization and
1023 cloning of tensilin, the collagen-fibril binding and tissue-stiffening factor from *Cucumaria*
1024 *frondosa* dermis. *Matrix Biol*, 21, 625-35.

- 1025 Trotter JA, Lyons-Levy G, Chino K, et al. (1999). Collagen fibril aggregation-inhibitor from sea
1026 cucumber dermis. *Matrix Biol*, 18, 569-78.
- 1027 Trotter JA, Lyons-Levy G, Luna D, et al. (1996). Stiparin: a glycoprotein from sea cucumber
1028 dermis that aggregates collagen fibrils. *Matrix Biol*, 15, 99-110.
- 1029 Trotter JA, Thurmond FA & Koob TJ (1994). Molecular structure and functional morphology of
1030 echinoderm collagen fibrils. *Cell and tissue research*, 275, 451-8.
- 1031 Wilkie IC (1996). Mutable collagenous structure or not? A comment on the re-interpretation by del
1032 Castillo et al of the catch mechanism in the sea urchin spine ligament. *Biol Bull-U*s, 190,
1033 237-242.
- 1034 Wilkie IC (2001). Autotomy as a prelude to regeneration in echinoderms. *Microscopy research and*
1035 *technique*, 55, 369-396.
- 1036 Wilkie IC (2002). Is muscle involved in the mechanical adaptability of echinoderm mutable
1037 collagenous tissue? *J Exp Biol*, 205, 159-65.
- 1038 Wilkie IC (2005). Mutable collagenous tissue: overview and biotechnological perspective. *Progress*
1039 *in molecular and subcellular biology*, 39, 221-50.
- 1040 Wilkie IC, Emson RH & Mladenov PV (1995). Autotomy mechanisms and its control in the starfish
1041 *Pycnopodia helianthoides* (Brandt). In: Emson SaC (ed.) *Echinoderm Research 1995*.
1042 Rotterdam: Balkema.
- 1043 Yamada A, Tamori M, Iketani T, Oiwa K & Motokawa T (2010). A novel stiffening factor inducing
1044 the stiffest state of holothurian catch connective tissue. *The Journal of experimental biology*,
1045 213, 3416-22.
- 1046 Yang W, Sherman VR, Gludovatz B, et al. (2015). On the tear resistance of skin. *Nat Commun*, 6,
1047 6649.
- 1048 Zamora S, Rahman IA & Smith AB (2012). Plated Cambrian bilaterians reveal the earliest stages of
1049 echinoderm evolution. *PloS one*, 7, e38296.
- 1050 Ziegler A, Faber C, Mueller S, Nagelmann N & Schröder L (2014). A dataset comprising 141
1051 magnetic resonance imaging scans of 98 extant sea urchin species. *GigaScience*, 3, 21-21.
- 1052 Ziegler A, Ogurreck M, Steinke T, et al. (2010). Opportunities and challenges for digital
1053 morphology. *Biology Direct*, 5, 45-45.
- 1054 Zimmermann EA, Schaible E, Bale H, et al. (2011). Age-related changes in the plasticity and
1055 toughness of human cortical bone at multiple length scales. *Proc Natl Acad Sci U S A*, 108,
1056 14416-21.
- 1057

1058

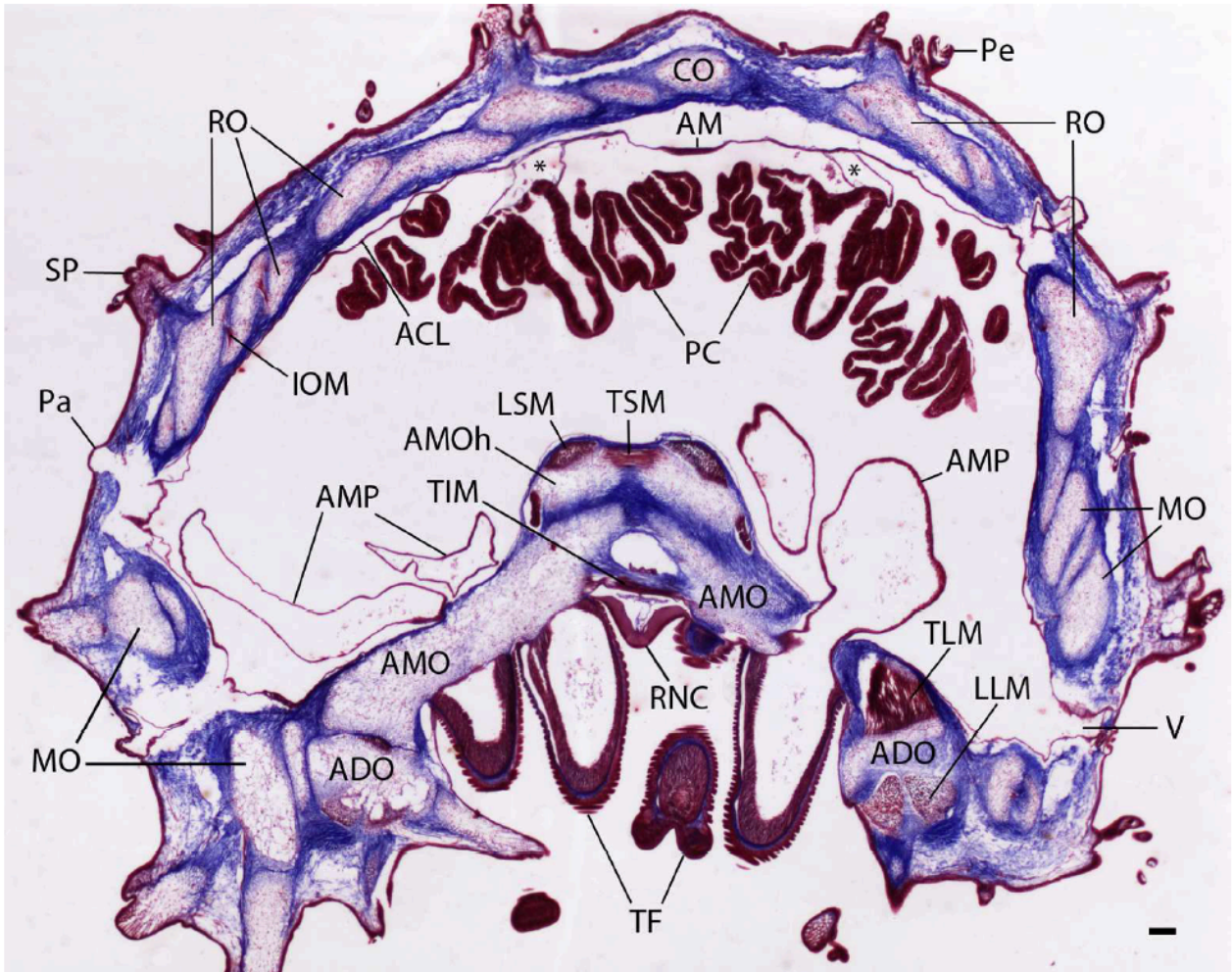
1059 Figure 1
1060



1061
1062

1063
1064
1065

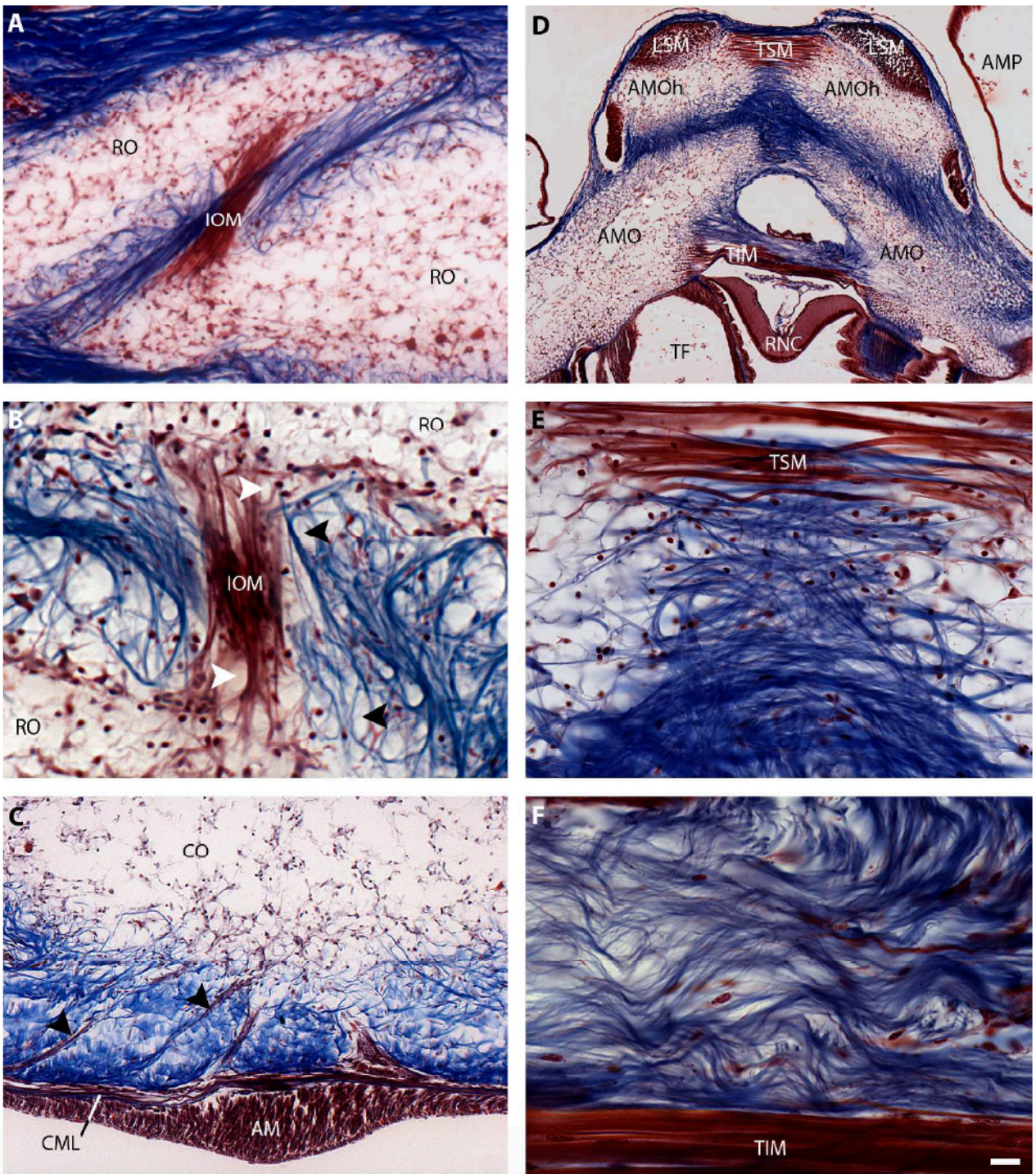
Figure 2



1066
1067

1068
1069
1070

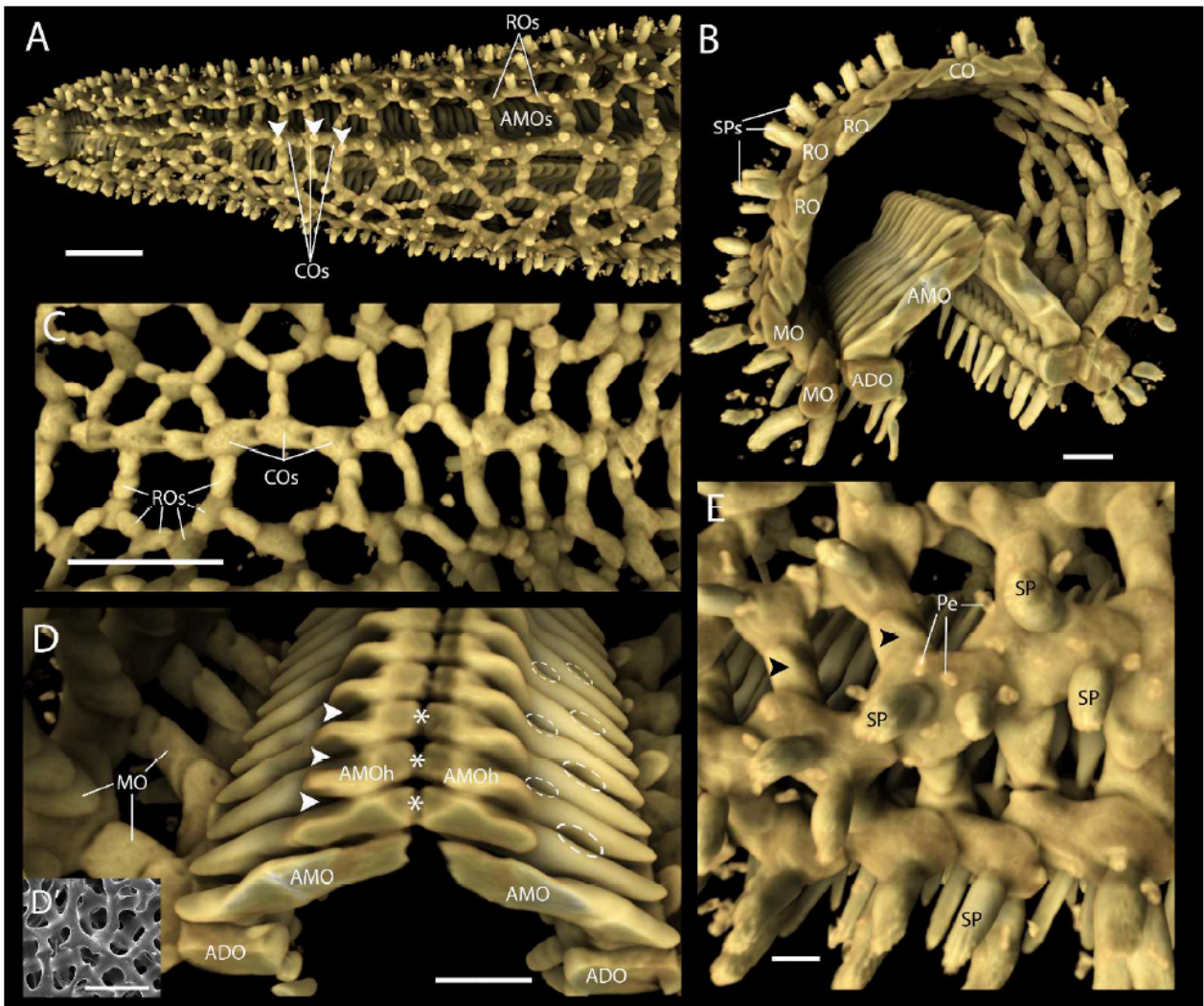
Figure 3



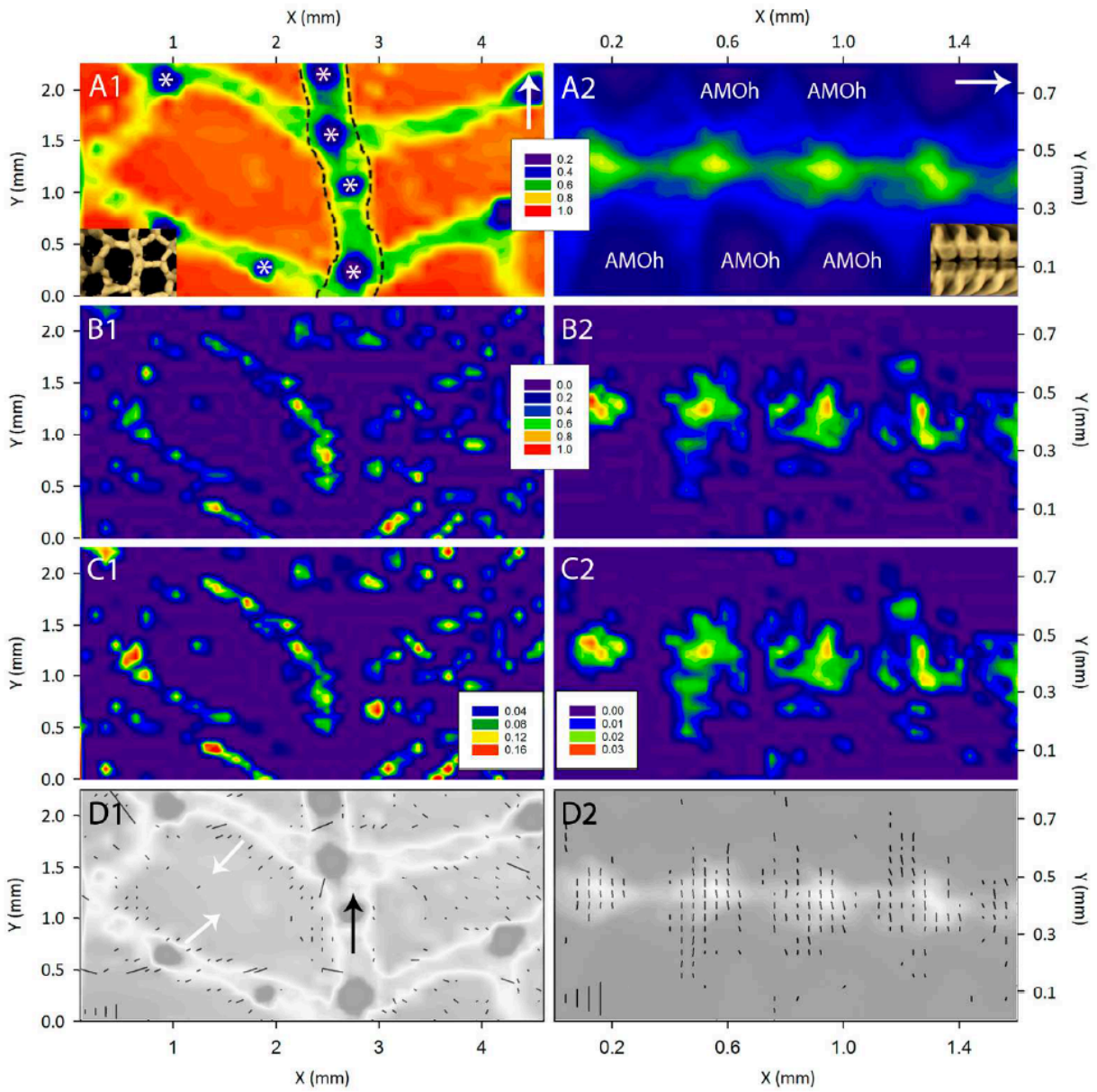
1071
1072

1073
1074
1075

Figure 4

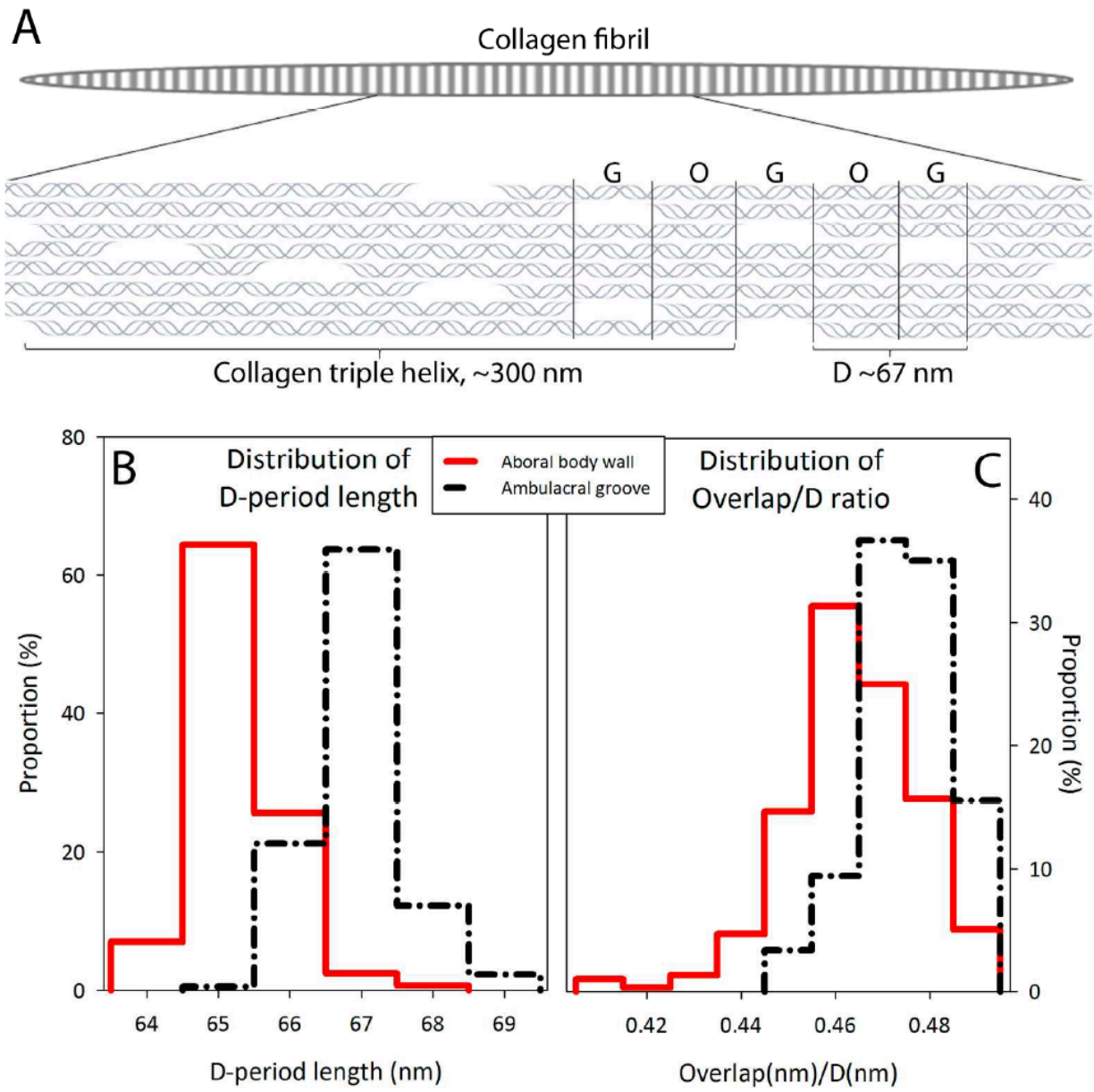


1076
1077



1082
1083
1084

Figure 6



1085
1086